Max-Planck-Institut
für Mathematik
in den Naturwissenschaften
Leipzig

Toward diagrammatic multiresolution
analysis for electron correlations

by

*Heinz-Jürgen Flad, Wolfgang Hackbusch,
Hongjun Luo, and Dietmar Kolb*

Toward diagrammatic multiresolution analysis for electron correlations

Heinz-Jürgen Flad and Wolfgang Hackbusch

Max-Planck-Institut für Mathematik in den Naturwissenschaften, Inselstr. 22-26, D-04103 Leipzig

Hongjun Luo and Dietmar Kolb

Institut für Physik, Universität Kassel, Heinrich-Plett-Str. 40, D-34132 Kassel

September 29, 2004

Abstract

We present a multiscale treatment of electron correlations based on hyperbolic wavelet expansions of Jastrow-type correlation functions. Wavelets provide hierarchical basis sets that can be locally adapted to the length- and energy-scales of physical phenomena. Combined with hyperbolic tensor products and local adaptive refinement near the inter-electron cusp, these wavelet bases enable sparse representations of Jastrow factors. The computational efficiency of wavelets in electronic structure calculations is demonstrated within the coupled electron-pair approximation (local ansatz). Based on a diagrammatic multiresolution analysis, we discuss various kinds of sparsity features for matrix elements required by the local ansatz. Sparsity originates from the hierarchical structure and vanishing moments property of wavelet bases. This led us to a recurrence scheme for the evaluation of matrix elements with almost linear computational complexity with respect to the size of the underlying isotropic 3d-wavelet basis. Numerical studies for selected diagrams are presented for a homogeneous electron gas.

1 Introduction

1.1 Wavelets in electronic structure calculations

The nonrelativistic Schrödinger equation within the Born-Oppenheimer approximation provides a firm basis for electronic structure calculations in quantum chemistry and solid state physics. Antisymmetry of fermionic wavefunctions introduces, via Pauli's exclusion principle, a multiscale structure into many-electron systems. This multiscale character expresses itself in the energy- and length-scales of electronic properties, extending over several orders of magnitude. Synergetic effects, caused by couplings between different scales, often prevent their separate treatment. In virtue of the multiscale character of many-electron systems, it is tempting to study possible applications of some recent mathematical developments in the field of multiscale analysis. Within the last two decades, tremendous progress has been made in multiscale methods [1], which became a central topic of applied mathematics with close relations to scientific computing. In particular wavelet based multiresolution analysis [2, 3, 4, 5] proved to be a useful tool, both from the analytical and computational point of view [6, 7, 8]. Wavelets represent stable multiscale basis sets that can be locally adapted according to the length- and energy-scales of physical phenomena under consideration. Depending on the specific application, these wavelet bases can be equiped with a variety of useful properties including compact support, (bi)orthogonality and vanishing moments [2]. Because of their approximation properties and hierarchical structure, wavelets provide efficient approximations for functions containing local singularities [5, 6]. Furthermore, sparse representations for a large class of operators, differential as well as integral operators including the Coulomb interaction, exist in wavelet bases [6, 9, 10, 11, 12, 13]. Not surprisingly, wavelets attracted considerable

attention in electronic structure theory. Most of these applications, however, have been done so far in the context of *density functional theory* (DFT) [14, 15, 16, 17, 18, 19, 20, 21, 22, 23, 24, 25, 26, 27, 28]. Within the DFT approach all many-particle aspects of the system are represented by an approximate exchange-correlation potential in the Kohn-Sham equation. Therefore, multiresolution analysis can just be applied to multiscale aspects of single-particle systems. For such systems, the most important multiscale features are variations of the electron density between atomic core and valence regions in molecules and solids. We have pursued a different approach based on the multiscale treatment of electron correlations. In our previous publications [29, 30] (hereafter called papers I and II, respectively), we have studied wavelet expansions of correlated wavefunctions, with special emphasize on the behaviour of the wavefunction near the inter-electron cusp. It turned out that wavelets provide sparse approximations of Jastrow-type correlation functions. However, the computational complexity for the computation of matrix elements posed severe limitations on the size of the systems. Within the present work we have studied the computational complexity of a simplified version of our approach using a combination of diagrammatic techniques and multiresolution analysis.

The paper is organized as follows: In Section 1.2 we give a brief overview of our approach to wavelet expansions of correlated wavefunctions. Taking a simple model problem for extended systems, in Section 1.3 some arguments are given in favour of a nonlinear exponential ansatz for the wavelet expansion. This lead us to an approximate treatment of electron correlations using the local ansatz briefly discussed in Section 1.4. In Section 2 we present a diagrammatic technique for the evaluation of matrix elements required by the local ansatz in a biorthogonal wavelet bases. The main part of our paper is devoted to a thorough discussion of the computational complexity of these matrix elements. This is done in three steps. In Section 2.1 we first estimate the cardinalities of various sets of diagrams, which appear within the evaluation of matrix elements. The estimates are solely based on the hierarchical structure and local character of wavelet bases. Following to these combinatorial arguments, in Section 2.2 we study the sparsity of certain sets of diagrams due to the vanishing moment property of wavelets. Such kind of sparsity can be extended to all sets of diagrams through a wavelet expansion of pointwise wavelet products, as it is outlined in Section 2.3. All together, these considerations lead to a recurrence scheme for the evaluation of matrix elements with almost linear complexity with respect to the size of the underlying 3d-wavelet basis. We conclude our paper in Section 3 with some numerical studies for a homogeneous electron gas, which demonstrate the feasibility of our approach in realistic applications.

1.2 Hyperbolic wavelet expansion of Jastrow factors

We are focusing on solutions of the stationary Schrödinger equation

$$\left[\sum_{i=1}^{N} \left(-\frac{1}{2} \Delta_i + V_{\text{ext}}(\mathbf{r}_i) \right) + \sum_{i<j} \frac{1}{|\mathbf{r}_i - \mathbf{r}_j|} \right] \Psi(\mathbf{r}_1, \mathbf{r}_2, \dots, \mathbf{r}_N) = E \, \Psi(\mathbf{r}_1, \mathbf{r}_2, \dots, \mathbf{r}_N), \qquad (1)$$

where the Hamiltonian includes Coulomb interactions between the electrons and an external potential due to the nuclei. Atomic units have been used throughout this paper. A natural framework for the representation of many-electron wavefunctions Ψ is the product ansatz

$$\Psi(\mathbf{r}_1, \mathbf{r}_2, \dots, \mathbf{r}_N) = \mathcal{F} \, \Phi(\mathbf{r}_1, \mathbf{r}_2, \dots, \mathbf{r}_N), \qquad (2)$$

where the correlation operator $\mathcal{F}$ acts on a mean-field solution Φ. In general, $\mathcal{F}$ has to be understood as a linear operator, who's specific properties must be derived from a many-body theory. Well known examples are wave-operators in many-body perturbation theory or coupled-cluster operators. At the present state of our project, we have adopted a simplified ansatz, where $\mathcal{F}(\mathbf{r}_1, \mathbf{r}_2, \dots, \mathbf{r}_N)$ represents a symmetric function of the electron coordinates, usually called Jastrow factor [31], which corrects for inadequacies of the mean-field solution Φ. Within our approach, we perform a hyperbolic wavelet expansion of the Jastrow factor.

This can be done using either a linear ansatz

$$\mathcal{F}\left(\mathbf{r}_1, \mathbf{r}_2, \ldots, \mathbf{r}_N\right) = \sum_p \sideset{}{'}\sum_{\mathbf{J}} \sum_{\mathbf{A}} f_{\mathbf{J},\mathbf{A}}^{(p)} \; \mathcal{F}_{\mathbf{J},\mathbf{A}}^{(p)}\left(\mathbf{r}_1, \mathbf{r}_2, \ldots, \mathbf{r}_N\right), \tag{3}$$

or an exponential ansatz

$$\mathcal{F}\left(\mathbf{r}_1, \mathbf{r}_2, \ldots, \mathbf{r}_N\right) = \exp\left[\sum_p \sideset{}{'}\sum_{\mathbf{J}} \sum_{\mathbf{A}} f_{\mathbf{J},\mathbf{A}}^{(p)} \; \mathcal{F}_{\mathbf{J},\mathbf{A}}^{(p)}\left(\mathbf{r}_1, \mathbf{r}_2, \ldots, \mathbf{r}_N\right)\right], \tag{4}$$

where symmetrized wavelet tensor products ($\mathcal{F}^{(0)} := 1$)

$$\begin{aligned}
\mathcal{F}_{j,\mathbf{a}}^{(1)}\left(\mathbf{r}_1, \mathbf{r}_2, \ldots, \mathbf{r}_N\right) &= \gamma_{j,\mathbf{a}}^{(s)}(\mathbf{r}_1) + \gamma_{j,\mathbf{a}}^{(s)}(\mathbf{r}_2) + \cdots + \gamma_{j,\mathbf{a}}^{(s)}(\mathbf{r}_N), \\
\mathcal{F}_{\mathbf{J},\mathbf{A}}^{(2)}\left(\mathbf{r}_1, \mathbf{r}_2, \ldots, \mathbf{r}_N\right) &= \gamma_{j_1,\mathbf{a}_1}^{(s_1)}(\mathbf{r}_1)\, \gamma_{j_2,\mathbf{a}_2}^{(s_2)}(\mathbf{r}_2) + \cdots + \gamma_{j_1,\mathbf{a}_1}^{(s_1)}(\mathbf{r}_{N-1})\, \gamma_{j_2,\mathbf{a}_2}^{(s_2)}(\mathbf{r}_N), \\
&\vdots
\end{aligned} \tag{5}$$

are formed from isotropic 3d-wavelets $\gamma_{j,\mathbf{a}}^{(s)}(\mathbf{r})$. Concerning the construction of these wavelets from univariate wavelets and scaling functions, and for further details of our notation we refer to Appendix A. In those cases where details concerning type, level and location of wavelets are not relevant, we use single Greek wavelet indeces (γ_α) to simplify our notation. Capital Latin and Greek multi-indices are used to denote arrays of indices of the same kind like in the case of the tensor products (5). A prime on the sum with respect to the multilevel-index $\mathbf{J}$ in the expansions (3) and (4) indicates that only those tensor products are taken into account, which either satisfy the sparse grid condition for hyperbolic wavelets [32] or belong to the diagonal refinement along the electron-electron cusp, cf. papers I, II for details. The sparse grid condition for the multilevel-index $\mathbf{J}$ can be expressed as a constraint on the shifted sum of wavelet levels

$$|\mathbf{J}| := \sum_{i=1}^p (j_i - l_0 + 1) \le \tilde{Q}, \tag{6}$$

where p is the number of 3d-wavelets in the tensor products (5) and j_i are their corresponding levels. According to relation (6), the sparse grid threshold parameter $\tilde{Q}$ determines the possible combinations of 3d-wavelet levels that are taken into account in the tensor product expansions (3) and (4), starting at the coarsest level l_0 which appears in the isotropic 3d-wavelet basis. Optionally on the coarsest level, 3d-scaling functions $\beta_{l_0,\mathbf{a}}$ can be added to the wavelet basis. These functions represent contributions from wavelet levels $j < l_0$. Therefore, in relation (6) we have to assign to them a formal level $j_i = l_0 - 1$. As a consequence of the sparse grid condition, the number of tensor products in the p-electron correlation part of the expansions (3) and (4) is of $O(M \log(M)^{p-1})$ with respect to the cardinality M of the underlying 3d-wavelet basis. For small p, the growth is almost linear in M, however, it still increases exponentially with respect to p. As a consequence we can achieve only modest values of p in the expansions (3) and (4).

1.3 Size-consistency error for the linear ansatz

The linear hyperbolic wavelet expansion of the Jastrow factor (3) enables a strictly variational treatment of Schrödinger's equation. Applying Rayleigh-Ritz's variational principle yields a generalized eigenvalue problem

$$\sum_q \sum_\Lambda \langle \mathcal{F}_\Omega^{(p)} H \, \mathcal{F}_\Lambda^{(q)} \rangle f_\Lambda^{(q)} = E \sum_q \sum_\Lambda \langle \mathcal{F}_\Omega^{(p)} \mathcal{F}_\Lambda^{(q)} \rangle f_\Lambda^{(q)}, \tag{7}$$

with respect to the variational parameters $f_\Lambda^{(p)}$. To simplify our notation we have introduced a shorthand notation $\langle \cdots \rangle := \langle \Phi_{\mathrm{HF}} | \cdots | \Phi_{\mathrm{HF}} \rangle$ for expectation values with respect to the *Hartree-Fock* (HF) wavefunction. The linear ansatz avoids any uncontrolled approximations and is appropriate for benchmark

calculations on small systems. For typical applications to extended systems, however, a constant relative accuracy is required, independently of the size of the system. Within the linear ansatz, size-consistency [1] is hard to achieve and becomes a major issue for such kind of approach [33]. Not only an inflationary number of variational parameters, but even more severe, an increasing complexity of the matrix elements makes the linear hyperbolic wavelet expansion to a challenging problem for large systems. It has been already demonstrated by one of us [34], that in order to keep the computational complexity under control an additional constraint has to be imposed. Besides the sparse grid condition, we have to truncate the first sum in the expansion (3) at $p \leq p_{\max} \ll N$, where $p_{\max}$ may slightly vary with the size of the system. This resembles to truncation schemes for the *configuration interaction* (CI) method in quantum chemistry, where typically only *single and double excitations* (SDCI) are taken into account.

In order to illustrate this problem, we have studied the size-consistency error of hyperbolic wavelet expansions for a standard benchmark problem in quantum chemistry, namely systems of N noninteracting helium atoms. Such kind of model recovers essential physical aspects of the problem [35]. Due to Pauli's principle, molecules can roughly be described by interacting electron pairs. The dominant intra-pair interactions are taken into account by this model, whereas inter-pair correlation effects are excluded. The latter are more subtle and not easily accessible to analysis. For the sake of computational simplicity, we consider a standard wavelet tensor product expansion for a single helium atom

$$\Psi_{\text{He}} \left(\mathbf{r}_1, \mathbf{r}_2 \right) = \left[\sum_{p=0}^{2} \sum_{\mathbf{J}} \sum_{\mathbf{A}} f_{\mathbf{J},\mathbf{A}}^{(p)} \ \mathcal{F}_{\mathbf{J},\mathbf{A}}^{(p)} \left(\mathbf{r}_1, \mathbf{r}_2 \right) \right] \phi(\mathbf{r}_1) \, \phi(\mathbf{r}_2), \tag{8}$$

where we refer to paper I for further details. The corresponding wavefunction for a cluster of N noninteracting helium atoms is given by the product

$$\Psi_{\text{He}_N} \left(\mathbf{r}_1 \ldots \mathbf{r}_{2N} \right) = \prod_{i=1}^{N} \Psi_{\text{He}} \left(\mathbf{r}_{2i-1}, \mathbf{r}_{2i} \right), \tag{9}$$

where we can neglect antisymmetry due to the absence of interactions between the atoms. Obviously, the total energy scales linear with the number of helium atoms $E_{\text{He}_N} = N E_{\text{He}}$. After some reordering of the product wavefunction (9), the wavelet tensor products for the cluster can be arranged like in the linear ansatz (3)

$$\overline{\mathcal{F}}_{\mathbf{J},\mathbf{A}}^{(p)} \left(\mathbf{r}_1 \ldots \mathbf{r}_{2N} \right) = \prod_{i=1}^{N} \mathcal{F}_{\mathbf{J}_i,\mathbf{A}_i}^{(p_i)} \left(\mathbf{r}_{2i-1}, \mathbf{r}_{2i} \right), \qquad \text{with} \ \ p = \sum_i p_i, \tag{10}$$

except that permutational symmetry with respect to an interchange of variables among two different helium atoms is not required. Applying the hyperbolic wavelet approximation to the reordered wavefunction

$$\Psi_{\text{He}_N} \left(\mathbf{r}_1 \ldots \mathbf{r}_{2N} \right) \approx \left[\sum_{p} \sum_{|\mathbf{J}| \leq \tilde{Q}} \sum_{\mathbf{A}} \overline{f}_{\mathbf{J},\mathbf{A}}^{(p)} \ \overline{\mathcal{F}}_{\mathbf{J},\mathbf{A}}^{(p)} \left(\mathbf{r}_1 \ldots \mathbf{r}_{2N} \right) \right] \prod_{i=1}^{N} \phi(\mathbf{r}_{2i-1}) \, \phi(\mathbf{r}_{2i}), \tag{11}$$

only those tensor products $\overline{\mathcal{F}}_{\mathbf{J},\mathbf{A}}^{(p)}$ are taken into account for which the sparse grid condition (6) is satisfied. On each level of truncation $\tilde{Q}$, the coefficients $\overline{f}_{\mathbf{J},\mathbf{A}}^{(p)}$ have to be reoptimized with respect to the energy. In order to limit the computational effort, we have contracted the atomic wavelet coefficients on each of the tensor product levels $\mathbf{J}$. This did not introduce any noticeable error into our calculations. In Fig. 1 we have shown the size consistency error per atom $\Delta E = E_{\text{He}_N}/N - E_{\text{He}}$ in the case of a two-scale wavelet expansion on a single helium atom. We refer to paper I for further details concerning this wavefunction. For both thresholds $\tilde{Q} = 4, 6$, a single helium atom can afford all tensor products in the wavefunction (8), however, for clusters of several helium atoms, restrictions with respect to the full product wavefunction (9)

---

[1] In the terminology of quantum chemistry this property is often called size-extensivity.
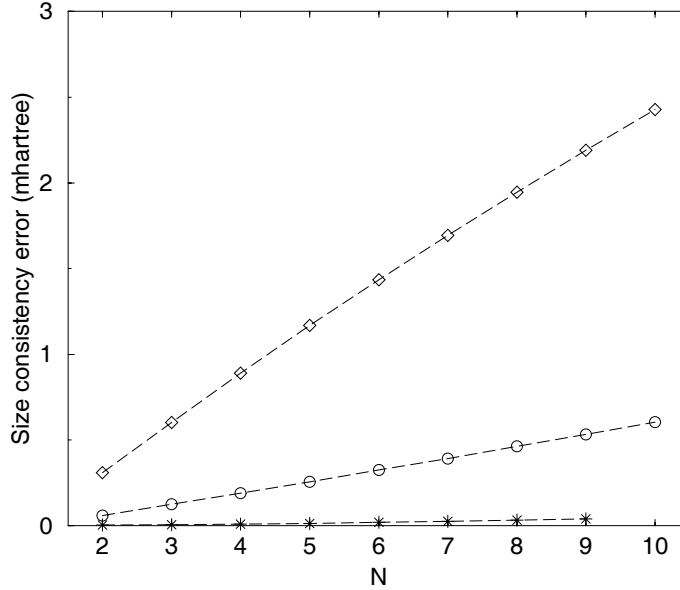
Figure 1: Size consistency error per atom $\Delta E = E_{\mathrm{He}_N}/N - E_{\mathrm{He}}$ (mhartree) of hyperbolic wavelet and SDCI approximations for systems of noninteracting helium atoms. The wavelet expansion for the Jastrow factor of a single helium atom has been taken from paper I (E_{He} = -2.89904 hartree, two levels $l_0 = -2, l_1 = -1$). Two different sparse grid constraints $\tilde{Q} = 4$ ($\circ$) and $\tilde{Q} = 6$ ($*$) have been imposed to the product wavefunction of the helium clusters. For comparison SDCI calculations ($\diamond$) have been performed with a s, p VQZ basis set (E_{He} = -2.90015 hartree).

are imposed. The hyperbolic wavelet approximation is less stringent than SDCI, in a sense that certain multicenter tensor products are still possible. For illustration we compare in Fig. 1 with SDCI calculations in a s, p *valence quadruple zeta* (VQZ) basis set [36]. It can be seen that the size consistency error is much smaller already for $\tilde{Q} = 4$ compared to the SDCI method. Increasing the sparse grid parameter to $\tilde{Q} = 6$ results in a very small size consistency error, which seems to be acceptable for systems with up to twenty electrons. In principle it appears to be possible, to adjust the parameter $\tilde{Q}$ to the system size in order to achieve a given accuracy. However in view of the difficulties concerning the evaluation of matrix elements, this becomes impracticable beyond a certain size of the system. For the sake of computational simplicity, we therefore have to abandon a rigorous treatment of the variational principle.

1.4   Local ansatz for electron correlations

In contrast to the linear ansatz (3), it is always possible to truncate the wavelet tensor product expansion in the exponential ansatz (4) at any value $2 \leq p_{\max} \leq N$, without violating size consistency for a system of noninteracting helium atoms. The essential drawback of the exponential ansatz (4) is, however, that a rigorous variational treatment is almost unfeasible due to its highly nonlinear character. Instead it is possible, to derive approximation schemes, where noninteracting electron-pairs are properly taken into account. Most prominent examples in quantum chemistry are the *coupled electron-pair approximation* (CEPA) [37] and *coupled cluster* (CC) theory [35]. A common feature of these methods is the decomposition of a one-particle Hilbert space into a subspace spaned by the occupied orbitals of the HF reference wavefunction and an orthogonal subspace spaned by virtual orbitals, which provide a basis for the treatment of electron correlations. Such kind of decomposition is not compatible with a hierarchical wavelet basis. A possible resolution to this problem, commonly employed in local correlation methods [38, 39, 40], is to orthogonalize all basis functions with respect to the occupied orbitals. However such kind of procedure destroys the multiscale relations underlying the fast wavelet transform and other wavelet specific

properties like vanishing moments.

As a consequence, we have to deviate from the standard many-particle treatment and use methods instead, which do not rely on any orthogonalization requirement. Such kind of methods are for example Krotscheck's *Fermi hypernetted chain* (FHNC) method [41, 42] and the local ansatz of Stollhoff and Fulde [43, 44]. The FHNC theory provides a hierarchical system of equations for an approximate treatment of the nonlinear variational problem, which is closely related to CC theory [45]. Originally developed for homogeneous systems in nuclear and condensed matter physics [31], the method has been generalized by Krotscheck to inhomogeneous systems [42, 46]. Applications in electronic structure theory range from the homogeneous electron gas [41] to metallic surfaces [46] and atoms [47, 48]. The FHNC method relies on diagrammatic techniques, which we have adopted with slight modifications for our purposes. Instead of classifying diagrams solely according to topological and structural criteria, we have introduced additional elements from multiresolution analysis. Standard diagrams comprise different types of correlations where the corresponding length- and energy-scales can vary over several orders of magnitude. Therefore it is often difficult to judge the significance of a specific diagram for a certain type of correlation. Within our approach, we further split these diagrams, via wavelet decompositions, into the various length- and energy-scales involved.

Without additional symmetries, the nonlinear system of FHNC equations is still very challenging from a computational point of view and we refrain from a numerical treatment within multiresolution analysis. Instead, we take a simplified many-particle method, the local ansatz, which is essentially equivalent to a specific version of the *coupled electron pair approximation* (CEPA0). Furthermore, the local ansatz can be considered as a certain type of approximation within the projection method of Becker and Fulde [49, 50], which comprises an essentially exact many-particle scheme based on operator expansions in Liouville space. Together with the diagrammatic framework developed within the FHNC method, the local ansatz seems to provide a natural starting point for the envisaged multiresolution diagrammatic analysis of electron correlations in extended systems.

Within the simplest version of the local ansatz only two-particle correlation operators $\mathcal{F}_\Lambda^{(2)}$ are taken into account, which have to satisfy the admissibility conditions

$$\langle \mathcal{F}_\Lambda^{(2)} \rangle = 0, \qquad \langle H_1 \mathcal{F}_\Lambda^{(2)} \rangle \neq 0, \tag{12}$$

where the residual interaction $H_1 := H - H_{\mathrm{SCF}}$ is defined as the difference between the exact and HF Hamiltonian. The local ansatz corresponds to a linear system of equations [50]

$$\langle \mathcal{F}_\Omega^{(2)\dagger} H_1 \rangle + \sum_\Lambda \left(\langle \mathcal{F}_\Omega^{(2)\dagger} H \mathcal{F}_\Lambda^{(2)} \rangle - \langle \mathcal{F}_\Omega^{(2)\dagger} \mathcal{F}_\Lambda^{(2)} \rangle \langle H \rangle \right) f_\Lambda = 0, \tag{13}$$

where the correlation energy is given by the expression

$$E_{\mathrm{corr}} = \sum_\Lambda \langle H_1 \mathcal{F}_\Lambda^{(2)} \rangle f_\Lambda. \tag{14}$$

A comparison of Eq. (13) with the generalized eigenvalue equation (7), shows that the local ansatz requires the same type of matrix elements as a variational treatment of the linear expansion (3) restricted to two-particle terms. The essential difference between both methods, however, is that the matrix elements in Eq. (13) appear in form of cumulants, cf. the first admissibility condition (12). This property is sufficient to guarantee size-consistency for the local ansatz [49].

2 Diagrammatic evaluation of matrix elements

A significant advantage of the local ansatz is its great flexibility concerning the specific choice of the correlation operators. Whereas the FHNC method is essentially limited to Jastrow-type correlation functions,

no such restriction exists for the local ansatz. Various types of correlation operators have been discussed in the literature [44, 49]. Conveniently expressed in terms of second quantization, these operators comprise inter-electronic spin couplings and on-site interactions similar to the Gutzwiller wavefunction. It is tempting to integrate such kind of operators in the framework of multiresolution analysis. Therefore, we first discuss the general case of an arbitrary two-particle correlation operator $\hat{\mathcal{F}}^{(2)}$ in second quantization, which is indicated by a hat on top of the operator. This requires only a slight modification of our notation to the effect that we have to add a spin degree of freedom to the wavelets $\gamma^{(s)}_{j,\mathbf{a}\uparrow}(\mathbf{r},\sigma)$, $\gamma^{(s)}_{j,\mathbf{a}\downarrow}(\mathbf{r},\sigma)$ and Greek indices now also imply the spin $\uparrow\downarrow$ assigned to a wavelet. Defining creation and annihilation operators $\hat{\gamma}^{\dagger}_{\alpha}$, $\hat{\gamma}_{\mu}$ with respect to a biorthogonal wavelet basis, we can express any two-particle correlation operator in the form

$$\hat{\mathcal{F}}^{(2)} = \frac{1}{2} \sum_{\alpha,\beta,\nu,\mu} \langle \tilde{\gamma}_{\alpha}\, \tilde{\gamma}_{\beta} | \mathcal{F}^{(2)} | \tilde{\gamma}_{\nu}\, \tilde{\gamma}_{\mu} \rangle\, \hat{\gamma}^{\dagger}_{\alpha}\, \hat{\gamma}^{\dagger}_{\beta}\, \hat{\gamma}_{\mu}\, \hat{\gamma}_{\nu}, \tag{15}$$

where the dual basis $\tilde{\gamma}_{\alpha}$ ($\langle \gamma_{\alpha} | \tilde{\gamma}_{\beta} \rangle = \delta_{\alpha,\beta}$) only enters into the operator amplitudes. For a Jastrow-type correlation function these amplitudes are given by

$$\langle \tilde{\gamma}_{\alpha}\, \tilde{\gamma}_{\beta} | \mathcal{F}^{(2)} | \tilde{\gamma}_{\nu}\, \tilde{\gamma}_{\mu} \rangle = \sum_{\sigma_1,\sigma_2} \int dr_1^3 \int dr_2^3\, \tilde{\gamma}_{\alpha}(\mathbf{r}_1,\sigma_1)\, \tilde{\gamma}_{\beta}(\mathbf{r}_2,\sigma_2)\, \mathcal{F}^{(2)}(\mathbf{r}_1,\mathbf{r}_2)\, \tilde{\gamma}_{\nu}(\mathbf{r}_1,\sigma_1)\, \tilde{\gamma}_{\mu}(\mathbf{r}_2,\sigma_2) \tag{16}$$

Applying Wick's theorem, the operator (15) splits into two parts

$$\hat{\mathcal{F}}^{(2)} = \left\{ \overbracket{\hat{\mathcal{F}}^{(2)}} \right\} + \left\{ \hat{\mathcal{F}}^{(2)} \right\}, \tag{17}$$

where curly brackets indicate normal ordering with respect to the HF reference wavefunction (see Appendix B for details). The first term on the right hand side contains all possible single and double internal contractions of the operator. Following Becker and Fulde [50], we restrict our two-particle correlation operators to the normal ordered part of Eq. (17), in order to get rid of a constant term and possibly redundant one-particle contributions. By this construction, the first admissibility condition (12) is automatically satisfied. According to its definition, the residual interaction

$$\hat{H}_1 := \hat{H} - \hat{H}_{\text{SCF}} = \langle \hat{H}_1 \rangle + \frac{1}{2} \sum_{\kappa,\lambda,\nu,\mu} \langle \tilde{\gamma}_{\kappa}\, \tilde{\gamma}_{\lambda} | r_{12}^{-1} | \tilde{\gamma}_{\nu}\, \tilde{\gamma}_{\mu} \rangle \left\{ \hat{\gamma}^{\dagger}_{\kappa}\, \hat{\gamma}^{\dagger}_{\lambda}\, \hat{\gamma}_{\mu}\, \hat{\gamma}_{\nu} \right\}, \tag{18}$$

essentially corresponds to the normal ordered product of the two-electron Coulomb interaction. Therefore, the second constraint (12) is generically satisfied.

Concerning the computational complexity of matrix elements, we focus on cumulants of the residual interaction (18). The cumulants

$$\langle \hat{\mathcal{F}}^{(2)\dagger}_{\Omega}\, \hat{H}_1\, \hat{\mathcal{F}}^{(2)}_{\Lambda} \rangle - \langle \hat{\mathcal{F}}^{(2)\dagger}_{\Omega}\, \hat{\mathcal{F}}^{(2)}_{\Lambda} \rangle \langle \hat{H}_1 \rangle = \tag{19}$$

$$\frac{1}{2} \sum_{\alpha,\beta,\zeta,\eta} \langle \tilde{\gamma}_{\alpha}\, \tilde{\gamma}_{\beta} | \mathcal{F}^{(2)}_{\Omega} | \tilde{\gamma}_{\zeta}\, \tilde{\gamma}_{\eta} \rangle^{*} \frac{1}{2} \sum_{\kappa,\lambda,\nu,\mu} \langle \tilde{\gamma}_{\kappa}\, \tilde{\gamma}_{\lambda} | r_{12}^{-1} | \tilde{\gamma}_{\nu}\, \tilde{\gamma}_{\mu} \rangle \frac{1}{2} \sum_{\xi,\rho,\sigma,\tau} \langle \tilde{\gamma}_{\xi}\, \tilde{\gamma}_{\rho} | \mathcal{F}^{(2)}_{\Lambda} | \tilde{\gamma}_{\sigma}\, \tilde{\gamma}_{\tau} \rangle$$

$$\times \left\langle \left\{ \hat{\gamma}^{\dagger}_{\zeta}\, \hat{\gamma}^{\dagger}_{\eta}\, \hat{\gamma}_{\beta}\, \hat{\gamma}_{\alpha} \right\} \left\{ \hat{\gamma}^{\dagger}_{\kappa}\, \hat{\gamma}^{\dagger}_{\lambda}\, \hat{\gamma}_{\mu}\, \hat{\gamma}_{\nu} \right\} \left\{ \hat{\gamma}^{\dagger}_{\xi}\, \hat{\gamma}^{\dagger}_{\rho}\, \hat{\gamma}_{\tau}\, \hat{\gamma}_{\sigma} \right\} \right\rangle$$

can be evaluated using Wick's theorem and the contraction rules derived in Appendix B. Using the diagrammatic techniques discussed in Refs. [49, 51, 52], these matrix elements are represented by the Goldstone diagrams shown in Fig. 2, where we have used the diagrammatic elements depicted in Fig. 3. These elements encompass two types of contractions (D_1, D_2) as well as Coulomb interactions (D_3) and operator amplitudes (D_4). For each Goldstone diagram in Fig. 2, a prefactor has been given consisting of a phase and symmetry factor according to the standard rules for Goldstone diagrams [52].

So far, we did not impose any restrictions on the specific form of the two-electron correlation operators (15). In the following, we restrict ourselves to Jastrow factors which are symmetric functions of the spatial
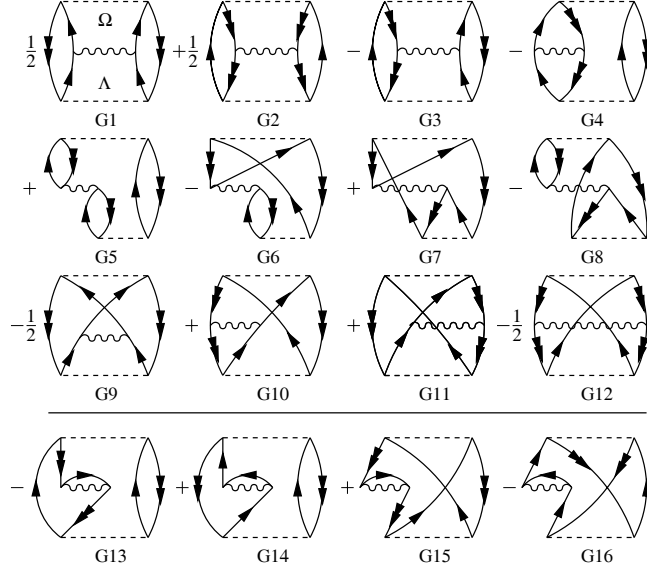
Figure 2: Goldstone diagrams for the cumulants of the two-body Coulomb interaction. The sum of diagrams G-1 to G-12 correspond to the cumulants of the residual interaction (19), whereas the remaining diagrams G-13 to G-16 emerge from the exchange part of H_{SCF}.

Figure 3: Diagrammatic elements for Goldstone diagrams in a biorthogonal wavelet basis.

electron coordinates. Since all ingredients of the local ansatz can be expressed as simple functions of the electron coordinates, we can use the resolution of the identity $\mathbb{I} = \sum_\alpha |\tilde{\gamma}_\alpha\rangle\langle\gamma_\alpha|$, in order to express our diagrammatic elements in terms of simple functions only. According to the modified setting, diagrams are expressed in position space using the diagrammatic elements E_1 to E_4, which are shown in Fig. 4. By a slight abuse of our notation (5), we have introduced the pair-correlation functions (E_4)

$$\mathcal{F}^{(2)}_{\alpha\beta}(\mathbf{r}_1, \mathbf{r}_2) = \gamma_\alpha(\mathbf{r}_1)\,\gamma_\beta(\mathbf{r}_2) + \gamma_\alpha(\mathbf{r}_2)\,\gamma_\beta(\mathbf{r}_1) \tag{20}$$

into our scheme. Spinless HF density matrices

$$\rho(\mathbf{r}_1, \mathbf{r}_2) = \sum_i n_i\,\phi_i(\mathbf{r}_1)\,\phi_i(\mathbf{r}_2)^*, \tag{21}$$

are represented in terms of spatial orbitals, where n_i is the occupation number of the i'th orbital. Each vertex in the diagrams corresponds to an integral $\int d^3r$. Due to the remaining spin degree of freedom, we have to assign an additional weight factor of 2^L, where L corresponds to the number of closed loops in a diagram. For our numerical analysis of the diagrams it is convenient to further evaluate all the lines with a double arrow. The resulting diagrams are closely related to Krotscheck's FHNC diagrams. Furthermore, we introduce symbols for single wavelets (E_5) and pointwise wavelet products (E_6) into our diagrammatic scheme.

8

E_1	$\mathbf{r}_2 \longrightarrow \mathbf{r}_1$	$\frac{1}{2}\rho(\mathbf{r}_1, \mathbf{r}_2)$
E_2	$\longrightarrow$	$\delta(\mathbf{r}_1 - \mathbf{r}_2) - \frac{1}{2}\rho(\mathbf{r}_1, \mathbf{r}_2)$
E_3	$\sim\!\!\sim\!\!\sim\!\!\sim$	r_{12}^{-1}
E_4	$\overset{\alpha\,\beta}{\succ\!\text{-------}\!\prec}$	$\mathcal{F}_{\alpha\beta}^{(2)}(\mathbf{r}_1, \mathbf{r}_2)$
E_5	$\alpha \diamondsuit$	$\gamma_\alpha(\mathbf{r})$
E_6	$\alpha \diamondsuit\!\!\diamondsuit \beta$	$\gamma_\alpha(\mathbf{r})\,\gamma_\beta(\mathbf{r})$

Figure 4: Diagrammatic elements for FHNC-like diagrams in position space.

2.1 Recurrence scheme for the evaluation of diagrams

It is common practice in solid state physics [53] and quantum chemistry [39, 40] to discuss the computational complexity of a method versus the size of the system. For this a constant relative accuracy of the method, with respect to the size of the system, has been assumed. Contrary to these considerations, we want to discuss computational complexity versus numerical accuracy for a fixed system size. Neglecting systematic errors inherent to almost all many-particle methods, we want to study interrelations between discretization errors and computational complexity for a given method. Furthermore, we focus exclusively on electron correlations and do not impose any localization requirements on the one-particle density matrix. This includes the case of very accurate calculations for small systems, as well as systems where the one-particle density matrix is only slowly decaying like in metals. For our present purpose it is therefore convenient to use the orbital representation of the one-particle density matrix (21). Provided that the density matrix of a system decays exponentially [53], it is possible to exploit this property within our method in a straightforward manner.

The hierarchical structure and vanishing moments property of wavelet bases offer the possibility of sparse multiscale representations for Jastrow factors and the Coulomb interaction. Within this section, we want to discuss how to take advantage of multiscale representations with respect to the evaluation of matrix elements shown in Fig. 2 in terms of Goldstone diagrams. According to our discussion in papers I and II, we approximate the Jastrow factor by a linear combination of symmetrized tensor products in a hierarchical wavelet basis. Within the local ansatz, we restrict ourselves to two-electron correlation functions $\mathcal{F}_{\alpha\beta}^{(2)}$, which correspond to symmetrized tensor products of isotropic 3d-wavelets. For our subsequent analysis of the diagrams it is convenient to further decompose the tensor products (20) into monomials

$$\mathcal{F}_{\alpha\beta}'(\mathbf{r}_1, \mathbf{r}_2) = \gamma_\alpha(\mathbf{r}_1)\,\gamma_\beta(\mathbf{r}_2). \tag{22}$$

Concerning the physical interpretation and adaptivity of wavelet expansions, the tensor products (20) seem to be an appropriate choice. It has been argued in papers I and II that adaptive wavelet expansions exhibit a pronounced transition between long- and short-range correlations. The first type of correlations is well described by hyperbolic 3d-wavelet tensor products, whereas for the second type of correlations, tensor products concentrate almost exclusively along the diagonal. However, there exists an interesting alternative approach based on fully anisotropic hyperbolic wavelets (see Appendix A for details). Despite some conceptual difficulties for adaptive wavelet expansions, fully anisotropic hyperbolic wavelets possibly allow for a considerably smaller number of basis functions, at least for the description of long-range correlations. For the sake of simplicity, we restrict our formal analysis of the computational complexity to isotropic 3d-wavelet tensor products (20). Nevertheless, we have also studied fully anisotropic wavelets in our numerical experiments.

As a starting point for our analysis, we take a cube which either contains the system as a whole like in the case of a molecule or corresponds to a supercell, with periodic boundary conditions imposed,

Table 1: Cardinalities of certain sets of pointwise and tensor products for isotropic 3d-wavelets.

Wavelet (tensor) product	Diagrammatic element	Cardinality
$\gamma_\alpha(\mathbf{r})$	$\Diamond$	M
$\gamma_\alpha(\mathbf{r})\,\gamma_\beta(\mathbf{r})$	$\Diamond\!\!\Diamond$	$O(M\log(M))$
$\mathcal{F}'_{\alpha\beta}\,(\mathbf{r}_1,\mathbf{r}_2)$	- - - - - - - -	$O(M\log(M))$
$\gamma_\alpha(\mathbf{r}_1)\,\mathcal{F}'_{\nu\mu}\,(\mathbf{r}_1,\mathbf{r}_2)$	$\Diamond$- - - - - -	$O(M^2)$
$\mathcal{F}'_{\alpha\beta}\,(\mathbf{r}_1,\mathbf{r}_2)\,\mathcal{F}'_{\nu\mu}\,(\mathbf{r}_2,\mathbf{r}_3)$	- - - $\vee$ - - -	$O(M^2\log(M))$
$\mathcal{F}'_{\alpha\beta}\,(\mathbf{r}_1,\mathbf{r}_2)\,\mathcal{F}'_{\nu\mu}\,(\mathbf{r}_1,\mathbf{r}_2)$	========	$O(M^2)$

for a solid. Within this cube we choose an isotropic 3d-wavelet basis $\{\gamma_\alpha\}$. Starting at a coarsest level l_0, the cardinality of the wavelet basis $M = \text{card}\{\gamma_\alpha\}$ grows exponentially $M = O(2^{3l})$ with the finest level l in the basis. To simplify our arguments, we do not consider any kind of adaptivity for this wavelet basis. In our recurrence scheme various types of wavelet products can occur. It is essential for our discussion of the computational complexity to study the cardinality of the corresponding sets of wavelet products. In the following, we just state the results and refer to Appendix C for further details. The set of pointwise wavelet products with overlapping supports has $\text{card}\{\gamma_\alpha(\mathbf{r}_1)\,\gamma_\beta(\mathbf{r}_2)\} = O(M\log(M))$. Following our line of arguments, we can approximate the two-particle Jastrow factor using hyperbolic 3d-wavelet tensor products with $\text{card}\{\mathcal{F}'_{\alpha\beta}\,(\mathbf{r}_1,\mathbf{r}_2)\} = O(M\log(M))$. At intermediate steps of the recurrence scheme, we have to consider the set of products between wavelets and hyperbolic tensor products, which has $\text{card}\{\gamma_\alpha(\mathbf{r}_1)\,\mathcal{F}'_{\nu\mu}\,(\mathbf{r}_1,\mathbf{r}_2)\} = O(M^2)$. The final diagrams contain products between hyperbolic tensor products, where we have to distinguish between one- and two-sided overlaps. In the first case we have $\text{card}\{\mathcal{F}'_{\alpha\beta}\,(\mathbf{r}_1,\mathbf{r}_2)\,\mathcal{F}'_{\nu\mu}\,(\mathbf{r}_2,\mathbf{r}_3)\} = O(M^2\log(M))$, which is slightly reduced to $\text{card}\{\mathcal{F}'_{\alpha\beta}\,(\mathbf{r}_1,\mathbf{r}_2)\,\mathcal{F}'_{\nu\mu}\,(\mathbf{r}_1,\mathbf{r}_2)\} = O(M^2)$ in the second case. For later reference, we have summarized these cardinalities in Table 1. It has been already mentioned that on fine levels, hyperbolic wavelet tensor products become less important and diagonal tensor products are getting dominant. Concerning the computational complexity, diagonal tensor products on fine levels require only minor additional computational effort. Further simplifications can be achieved through contraction schemes, which have been discussed in paper I and II. Therefore, we neglect the effect of diagonal refinement in our discussion of the recurrence scheme.

After these preparatory remarks, we start with developing a recurrence scheme, which finally leads to the matrix elements (19). Except the Coulomb interaction, all ingredients to build up diagrams are already represented by tensor product expansions. The Goldstone diagrams decompose into one- and two-electron integrals

$$\int d^3r\;\phi_i(\mathbf{r})\left[\begin{array}{c}1\\\gamma_\alpha(\mathbf{r})\end{array}\right]\left[\begin{array}{c}1\\\gamma_\beta(\mathbf{r})\end{array}\right]\phi_j(\mathbf{r}),\tag{23}$$

$$\int d^3r_1 \int d^3r_2 \, \phi_i(\mathbf{r}_1) \, \phi_j(\mathbf{r}_1) \begin{bmatrix} 1 \\ \gamma_\alpha(\mathbf{r}_1) \\ \gamma_\alpha(\mathbf{r}_1) \, \gamma_\beta(\mathbf{r}_1) \end{bmatrix} \frac{1}{\mid \mathbf{r}_1 - \mathbf{r}_2 \mid} \begin{bmatrix} 1 \\ \gamma_\mu(\mathbf{r}_2) \\ \gamma_\mu(\mathbf{r}_2) \, \gamma_\nu(\mathbf{r}_2) \end{bmatrix} \phi_k(\mathbf{r}_2) \, \phi_l(\mathbf{r}_2), \qquad (24)$$

where square brackets indicate various possible combinations of wavelets in the integrals. According to our previous discussion, only certain combinations of the wavelets within square brackets have to be taken into account. Further simplifications due to contractions of orbital indices appear. We start with eight basic sets of diagrams involving the Coulomb interaction, which are shown in Fig. 5. In these diagrams, wavelet indices and orbital indices assigned to external lines have been suppressed. The sets of diagrams 1 to 4 have four external lines with at most two wavelets on the vertices. Their overall cardinalities are $O(N^4)$, $O(N^4 M)$, $O(N^4 M^2)$ and $O(N^4 M \log(M))$, respectively. Diagrams of type 5 and 6 have only two external lines and three wavelets on the vertices, where two of them belong to a common hyperbolic tensor product $\mathcal{F}'_{\alpha\beta}$. Therefore, we obtain an overall $O(N^2 M^2)$ cardinality for these sets. The remaining sets of diagrams 7 and 8 have no external lines and two wavelets on each of the vertices, originating from a pair of hyperbolic tensor products $\mathcal{F}'_{\alpha\beta} \mathcal{F}'_{\nu\mu}$. According to Table 1, these sets have $O(M^2)$ cardinality. Concerning the sets of type 3,5,6,7, and 8 diagrams with wavelets or wavelet products on both vertices, we can distinguish two cases. In the first case, the supports of the wavelets or wavelet products on the two vertices overlap. The corresponding subsets have $O(N^4 M \log(M))$, $O(N^2 M \log(M)^2)$ and $O(M \log(M)^3)$ cardinalities, respectively. Further separation of the Coulomb interaction is not possible in this case. However in the second case, where the supports do not overlap, there is some chance for a further reduction of the computational complexity. In Section 2.2, we discuss some additional sparsity of the set of type 3 diagrams, that result from the vanishing moment property of wavelets (see Appendix A for an elementary discussion of this property). To a smaller extent such kind of sparsity can be also observed for the sets of type 5 and 6 diagrams. For the sets of type 7 and 8 diagrams with wavelet products on both vertices, the vanishing moment property does not work at all. Nevertheless it is possible to benefit in these cases from the vanishing moment property by performing a wavelet expansion of the wavelet products on the vertices. This topic is further discussed in Section 2.3, where we outline the necessary modifications of the recurrence scheme.

Summing up, we may say that the computational complexity of the basic diagrams involving Coulomb interactions increases at most quadratically with the number of wavelets. This assertion is based on combinatorial arguments taking into account a hyperbolic structure of the tensor products and the hierarchical character of wavelet bases. Beyond that our analysis shows that those diagrams where the Coulomb interaction cannot be further separated have almost linear complexity. Therefore it seems to be promising to further exploit the vanishing moments property in order to reduce the almost quadratic complexity for the treatment of electron correlations to linear complexity up to logarithmic factors.

In order to obtain the entire set of diagrams from the basic Coulomb diagrams, we first have to construct a recurrence scheme for some basic chain diagrams. These diagrams consist of chains of density matrices with wavelets or wavelet products on their vertices, that do not join the Coulomb interaction. The scheme outlined in Fig. 6 involves concatenations of chain diagrams with two external lines, which requires an $O(N)$ computational effort for each individual diagram. The cardinalities of sets of chain
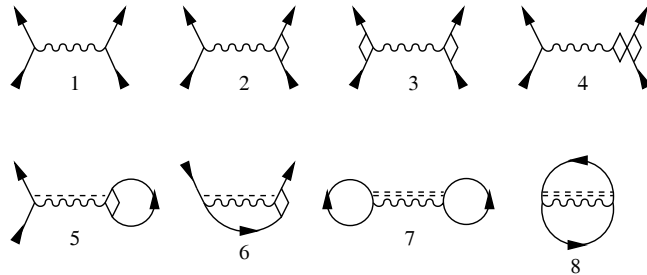

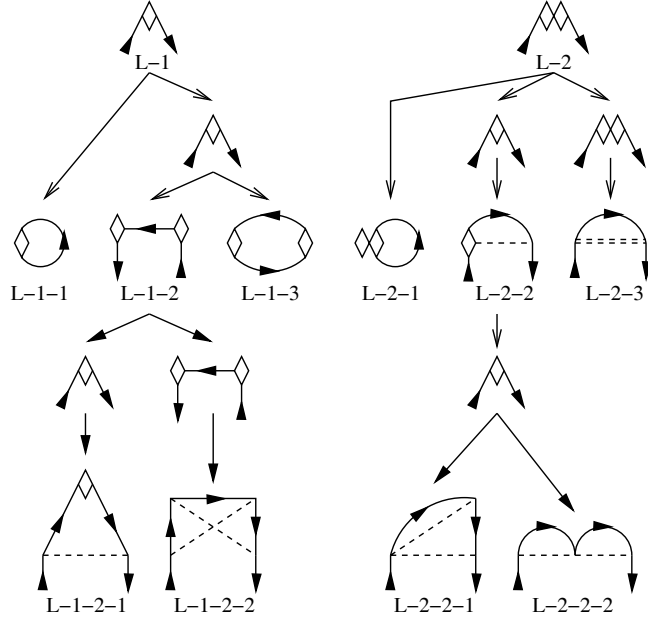Figure 5: Basic sets of diagrams involving the Coulomb interaction.

Figure 6: Basic sets of chain diagrams involving chains of density matrices with wavelets or wavelet products on the vertices.

diagrams ranges from $O(N^2M)$ to $O(N^2M^2\log(M)^2)$, as can be seen from Fig. 6. In order to simplify bookkeeping, our labeling of diagrams incorporates the tree-like structure of the recurrence scheme. Due to the smoothness of the density matrix, the vanishing moment property provides additional sparsity except for the sets of diagrams L-2, L-2-1 and L-2-3, where only wavelet products appear on the vertices. The first two sets of diagrams already have almost linear cardinalities with respect to the wavelet basis. For the set of diagrams L-2-3, however, it becomes necessary to perform a wavelet expansion of the wavelet products in order to benefit from the vanishing moment property. The product expansion can be also applied to the set of diagrams L-2-2-1 and L-2-2-2 with one wavelet product on the vertices.

Starting from the basic Coulomb diagrams, the entire recurrence scheme can be set up by successive concatenations with chain diagrams. To illustrate this scheme, Figs. 7 a, 8 show the descendants of the sets of basic type 1 to 6 diagrams. The final sets of diagrams (shown in Fig. 7 b) emerging from the set of type 1-1 diagrams represent contributions from the exchange part of H_{SCF}. A complete exposition of the remaining parts of the recurrence scheme is given in Appendix D. For sets of intermediate diagrams with two external lines, the cardinalities are at most $O(N^2M^2\log(M))$. At each individual step, where a set of open chain diagrams is concatenated with a set of diagrams involving four external lines, at most $O(N^4M^2\log(M))$ operations have to be performed. For a set of diagrams with two external lines this reduces to at most $O(N^2M^2\log(M)^2)$ operations. According to our previous discussion, all sets of diagrams for which the cardinality increases quadratically with the size of the wavelet basis, can benefit from further sparsity effects due to the vanishing moment property.

2.2 Sparse wavelet representation for certain classes of diagrams

The purpose of this section is to study the effect of vanishing moments (cf. Appendix A) on the sets of basic type 3, 5, and 6 diagrams and their descendants. So far we have tried to avoid in our presentation any reference to specific applications. Just a few general properties inherent to hierarchical wavelet bases have been employed. This was possible due to some universal features of Jastrow factors, which enable a sparse approximation in terms of hyperbolic wavelet tensor products with local refinement in the region of the inter-electron cusp. Expressed in the more general framework of multiresolution analysis [9, 10, 11, 12], we have used the asymptotic smoothness property of Jastrow factors, which means that an arbitrary function
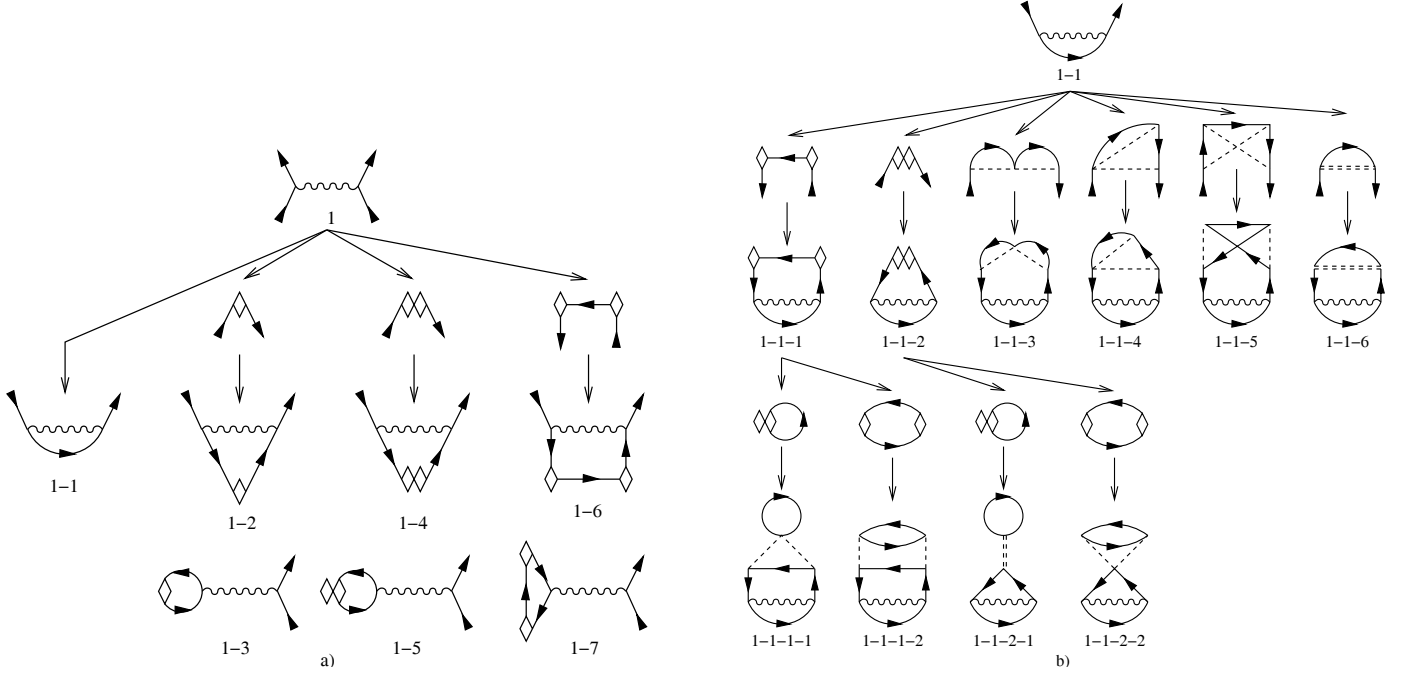
Figure 7: First step of the recurrence scheme for diagrams emerging from the set of basic type 1 diagrams (a) and all steps following the intermediate set of type 1-1 diagrams (b).

$A(\mathbf{r}_1, \mathbf{r}_2)$ has a sparse wavelet representation if its partial derivatives satisfy the inequalities

$$|\partial_{\mathbf{r}_1}^{\alpha} \partial_{\mathbf{r}_2}^{\beta} A(\mathbf{r}_1, \mathbf{r}_2)| \leq C_{\alpha,\beta} |\mathbf{r}_1 - \mathbf{r}_2|^{-(n+|\alpha|+|\beta|)}, \qquad \text{for} \ \ \mathbf{r}_1 \neq \mathbf{r}_2, \tag{25}$$

where the indices α, β correspond to any mixed partial derivatives of order $|\alpha|$ and $|\beta|$, respectively. Within the context of more complex diagrams, however, application of the vanishing moment property requires further considerations concerning the behaviour of the density matrix. Obviously, nuclear cusps or a highly oscillating behaviour of the density matrix within the support of a wavelet spoils this useful property. If such kind of behaviour is restricted to atomic core regions, which correspond to a comparatively small portion of the total volume, it can be handled by adaptive local refinements of the 3d-wavelet basis. Therefore, we neglect such kind of complications and essentially consider only valence electron systems, where core electrons have been replaced by pseudopotentials. A classical model for these systems is the homogeneous electron gas, where oscillations are bounded by the Fermi momentum k_F. This led us to a simplified model for basic type 3 diagrams

$$I_{j,l}^{(s,t)}(\mathbf{a}, \boldsymbol{\kappa}, \boldsymbol{\kappa}') = \int d^3 r_1 \int d^3 r_2 \, e^{-i\boldsymbol{\kappa}\mathbf{r}_1} \, \gamma_{j,\mathbf{a}}^{(s)}(\mathbf{r}_1) \, \frac{1}{|\, \mathbf{r}_1 - \mathbf{r}_2 \,|} \, e^{i\boldsymbol{\kappa}'\mathbf{r}_2} \, \gamma_{l,\mathbf{0}}^{(t)}(\mathbf{r}_2), \tag{26}$$

where only wavelets and the Coulomb interaction are left. All effects of the remainder of a diagram on the vertices are represented by plane waves, through which we can modulate the oscillations by varying the parameters $\boldsymbol{\kappa}, \boldsymbol{\kappa}'$. The presence of plane waves in the integrand has important consequences for the wavelet representation. Whereas the bare Coulomb interaction satisfies the asymptotic smoothness condition (25), this does not hold for its product with plane waves that appears in the integrals (26). The situation resembles to the kernel function of the Helmholtz equation, which is a well known problem in numerical analysis. In the following, we want to analyze the interplay of vanishing moments and oscillations for the integrals (26), which provide a fairly realistic model not only for basic type 3 diagrams but also for the basic type 5 and 6 diagrams. For the latter, we have to consider the mixed case of $I_{j,l}^{(s,0)}$ integrals, where a scaling function appears on one of the vertices.
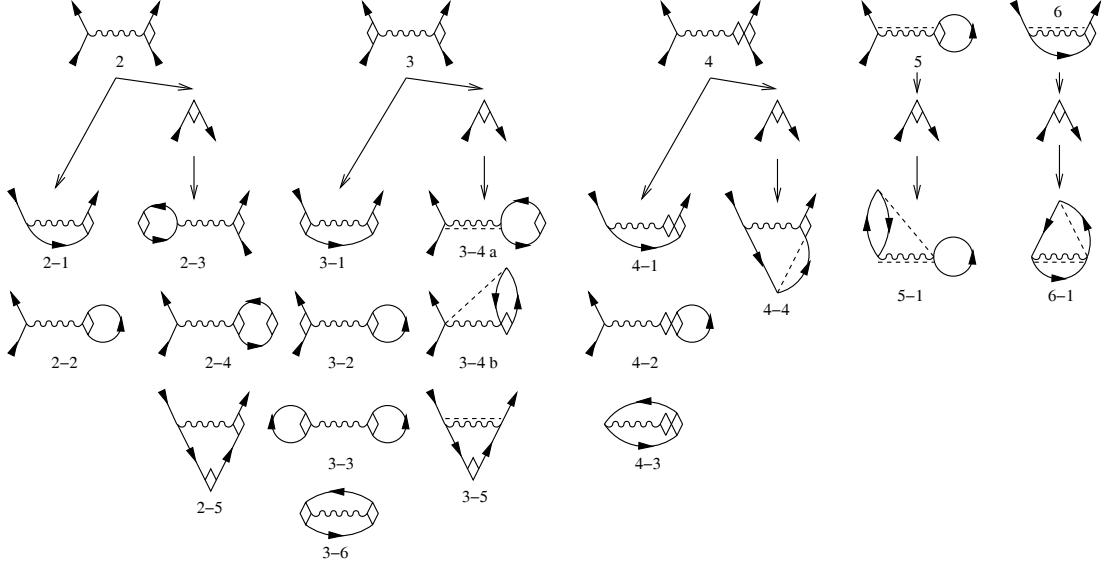
13

Figure 8: First step of the recurrence scheme for diagrams emerging from the sets of basic type 2 to 6 diagrams.

Calculation of the integrals (26) requires only minor modifications of the Gaussian transform method outlined in paper I. The integrals (26) can be expressed via the Gaussian transform method

$$I_{j,l}^{(s,t)}(\mathbf{a}, \boldsymbol{\kappa}, \boldsymbol{\kappa}') = \frac{2}{\sqrt{\pi}} \int_0^\infty dt \prod_{i=1}^3 G_{j,l}^{(s_i,t_i)}(\kappa_i, \kappa_i', a_i, t), \qquad (27)$$

in terms of the Fourier transform of the mother wavelet (scaling function) $\hat{\psi}^{(s)}(\omega) := \int dx\, e^{-i\omega x} \psi^{(s)}(x)$

$$\begin{aligned}
G_{j,l}^{(s_i,t_i)}(\kappa_i, \kappa_i', a_i, t) &= \int dx_1 dx_2\, e^{-i\kappa_i x_1} \psi_{j,a_i}^{(s_i)}(x_1)\, e^{-(x_1-x_2)^2 t^2}\, e^{i\kappa_i' x_2} \psi_{l,0}^{(t_i)}(x_2) \qquad (28) \\
&= \frac{2^{(j-l)/2}}{2\sqrt{\pi} t} e^{-i2^{-j}\kappa_i a} \int d\omega\, e^{i\omega a_i} \hat{\psi}^{(s_i)}(\omega - 2^{-j}\kappa_i)^* \, e^{-2^{2j}\omega^2/(4t^2)} \hat{\psi}^{(t_i)}\big(2^{(j-l)}\omega - 2^{-l}\kappa_i'\big),
\end{aligned}$$

where the functions (28) have been calculated following the procedure described in paper I. Results for various values of $\boldsymbol{\kappa}$ are shown in Fig. 9 (a). In agreement with our previous arguments, the vanishing moment property is destroyed by highly oscillating plane waves. Damping the oscillatory behaviour, we observe a faster decay of the integrals with respect to the distance between the wavelets. Vice versa, we obtain the same type of behaviour if we fix the value of $\boldsymbol{\kappa}$ and increase the levels of the wavelets instead.

In order to get a better understanding of the asymptotic behaviour of the integrals (26), we have performed a multipole expansion of the Coulomb interaction [54]

$$\begin{aligned}
\frac{1}{|\mathbf{r}_1 - \mathbf{r}_2 + \mathbf{b}|} &= \sum_l \frac{4\pi}{|\mathbf{b}|^{l+1}} \sum_{l'=0}^l (-1)^{l'} \left[\frac{4\pi}{(2l+1)(2l'+1)(2l-2l'+1)} \right]^{1/2} \sum_{m,m'}{}' Y_{l,m}(\phi_b, \theta_b)^* \quad (29) \\
&\times \left[\begin{pmatrix} l+m \\ l-l'+m-m' \end{pmatrix} \begin{pmatrix} l-m \\ l-l'-m+m' \end{pmatrix} \right]^{1/2} \mathcal{Y}_{l',m'}(\mathbf{r}_1)\, \mathcal{Y}_{l-l',m-m'}(\mathbf{r}_2),
\end{aligned}$$

where the prime on the third sum indicates the constraint $|m - m'| \le l - l'$. The functions $Y_{l,m}$, $\mathcal{Y}_{l,m}$ correspond to spherical harmonics and harmonic polynomials, respectively. In the case of disjoint supports of the wavelets in the integrals (26), we can perform the multipole expansion (29) with respect to the

center of the wavelet $\gamma_{j,\mathbf{a}}^{(p)}$ located at $\mathbf{b} = 2^{-j}\mathbf{a}$. From this expansion we obtain integrals of the form

$$\int d^3r \; \gamma_{j,\mathbf{0}}^{(s)}(\mathbf{r})\, e^{-i\boldsymbol{\kappa}\mathbf{r}}\, \mathcal{Y}_{l,m}(\mathbf{r}), \tag{30}$$

where the $\mathcal{Y}_{l,m}(\mathbf{r})$ are homogeneous polynomials of degree l in Cartesian coordinates. Therefore, these integrals factorize into one dimensional integrals

$$\int dx \; e^{-i\kappa_i x}\, \psi_{j,\mathbf{0}}^{(s_i)}(x)\, x^m = i^m \, 2^{-j/2} \frac{d^m \hat{\psi}^{(s_i)}(2^{-j}\kappa_i)}{d\kappa_i^m}, \qquad 0 \le m \le l, \tag{31}$$

which can be expressed in terms of derivatives of the Fourier transform of the mother wavelet or scaling function. The derivatives can be directly evaluated through successive derivation of the recurrence formulas

$$\hat{\psi}(\kappa) = \left(\sum_m g_m e^{-im\kappa/2}\right) \hat{\varphi}(\kappa/2), \qquad \hat{\varphi}(\kappa) = \left(\sum_m h_m e^{-im\kappa/2}\right) \hat{\varphi}(\kappa/2), \tag{32}$$

where g_m, h_m are the filter coefficients of the wavelet and scaling function, respectively. For a wavelet with n vanishing moments, the $(n-1)$'st derivatives vanish at the origin. Therefore, in the limit $j \to \infty$, a certain number of the coefficients (30) vanish, depending on the specific type of isotropic 3d-wavelet. Obviously, the magnitudes of $|\boldsymbol{\kappa}|$, $|\boldsymbol{\kappa}'|$ are crucial for the actual convergence to the limit. Convergence can be observed only if $2^{-j}|\kappa_i|$ is smaller than a certain critical value, as can be seen from Fig. 10, where the Fourier transform of a mother wavelet and its first and second derivatives are shown near the origin. In the presence of oscillations, the asymptotic behaviour at large distances between the wavelets, with levels j, l fixed, is governed by the monopole term in the expansion (29). This can be seen from Fig. 9 (b), where with decreasing magnitude of the oscillations, the asymptotic behaviour is approached at ever larger distances between the wavelets. It is interesting to see, that the multipole expansion already works for distances that are smaller than one could expect according to the diameters of the supports of the wavelets. Due to the fast spatial decay of the wavelets, we observed only very small contributions from overlapping regions beyond a certain distance. This means that for many practical purposes, we can work with effective diameters that are considerably smaller than the actual ones.

Summing up our previous discussion, it may be said, that the vanishing moment property provides additional sparsity for certain sets of basic diagrams. However, the actual degree of sparsity depends on the specific application and on the desired numerical accuracy. The former determines the magnitude of oscillations κ and the latter specifies the levels of resolution j in the wavelet expansion of the Jastrow factor. Only if the products $2^{-j}\kappa_i$ are sufficently small, we can expect a substantial sparsity due to vanishing moments for these sets of diagrams.

Before continuing our discussion of complex diagrams, we briefly want to consider the wavelet expansion of the density matrix itself. This shed some light on the sparsity of chain diagrams shown in Fig. 6. In general, we have to distinguish between metallic and nonmetallic systems. In the first case, the density matrices have polynomial decay with long-range oscillations, whereas in the second case exponential decay can be expected [53]. It has been observed by Goedecker and Ivanov [20] that in the second case sparse wavelet representations exist. For metals it is illustrative to consider the density matrix of a homogeneous electron gas

$$\rho(r_{12}) = \frac{3\rho}{2} \frac{\sin(k_F\, r_{12}) - k_F\, r_{12} \cos(k_F\, r_{12})}{(k_F\, r_{12})^3}, \tag{33}$$

which only depends on the inter-electron coordinate r_{12}. Due to the presence of oscillating terms, the density matrix (33) does not satisfy the asymptotic smoothness condition (25). As a consequence, wavelet and scaling function matrix elements have the same decay rates. However, the vanishing moment property has a large effect on the magnitude of the matrix elements. In contrast to our model problem (26), the density matrix (33) has no singularity along the diagonal. Therefore, absolute values of matrix elements
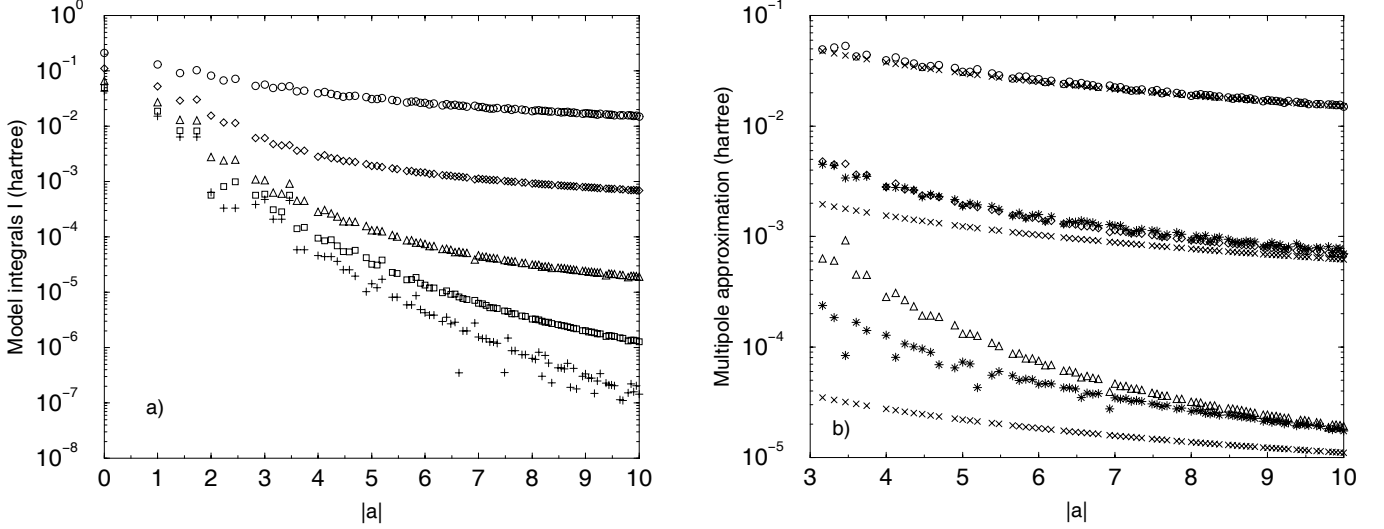
15

Figure 9: a) Model integrals $I_{j,l}^{(s,t)}(\mathbf{a}, \boldsymbol{\kappa}, \boldsymbol{\kappa}')$ for the basic type 3, 5, and 6 diagrams. Absolute values of the integrals $I_{0,0}^{(1,0)}(\mathbf{a}, \boldsymbol{\kappa}, \boldsymbol{\kappa})$ are plotted on a logarithmic scale versus the distance $|\mathbf{a}|$. The plane wave parameters (bohr^{-1}) were chosen to be isotropic $\kappa_1 = \kappa_2 = \kappa_3$ with values $\kappa_i = 2$ ($\circ$), $\kappa_i = 1$ ($\diamond$), $\kappa_i = 0.5$ ($\triangle$), $\kappa_i = 0.25$ ($\square$), $\kappa_i = 0$ ($+$). Isotropic 3d-wavelets and scaling functions were generated from the univariate SDD6 wavelet basis (see Appendix A). b) Multipole approximation of the integrals $I_{0,0}^{(1,0)}(\mathbf{a}, \boldsymbol{\kappa}, \boldsymbol{\kappa})$. Results for selected values of $\boldsymbol{\kappa}$ are shown for pure monopole $l = 0$ ($\times$) and up to quadrupole interactions $l = 2$ ($*$).

involving wavelets are uniformly smaller than pure scaling function matrix elements, as can be seen in Fig. 11. Concerning basic chain diagrams, this means that those diagrams are getting small, which have single wavelets on sufficiently fine levels on their vertices.

2.3   Wavelet expansion of pointwise wavelet products

Our previous discussion of the computational complexity of the recurrence scheme, mainly focused on the cardinalities of wavelets and their tensor products, where we have treated the number of electrons N as a constant parameter. Certain steps in the recurrent evaluation of the diagrams shown in Fig. 2, however, formaly scale like $O(N^2)$ or $O(N^4)$ with respect to the number of electrons. Although it is often possible to exploit the exponential decay of the density matrix in order to reduce the computational complexity up to linear scaling [53], there remain some important cases where this option fails. The most prominent example are metallic systems, where density matrices decay only algebraically like in the case of the homogeneous electron gas (33). Further examples are heavy atoms, which possess a fairly large number of electrons even in the valence shell. For such cases, the vanishing moments property remains the only possibility for a further reduction of the computational complexity. In order to work, the vanishing moments property requires single wavelets on the vertices of a diagram. However for almost half of the diagrams at least one pointwise wavelet product appears on their vertices. According to the hyperbolic tensor product structure of the monomials (22), most of them correspond to combinations of wavelets on distant scales. In the more favourable case, the wavelet which belongs to the coarser scale forms part of the product, whereas the wavelet on the finer scale contributes to a vertex individually. In such a case the vanishing moments property reduces the magnitude of the diagram. Because of the symmetric structure of the Jastrow factor, we also have to consider the less favourable case, where the single wavelet belongs to the coarser scale. Due to an increasing effect of orbital oscillations on the vanishing moments property of this wavelet, the corresponding diagram has typically a considerably larger magnitude.

A partial resolution to this problem can be provided through a wavelet expansion of pointwise wavelet
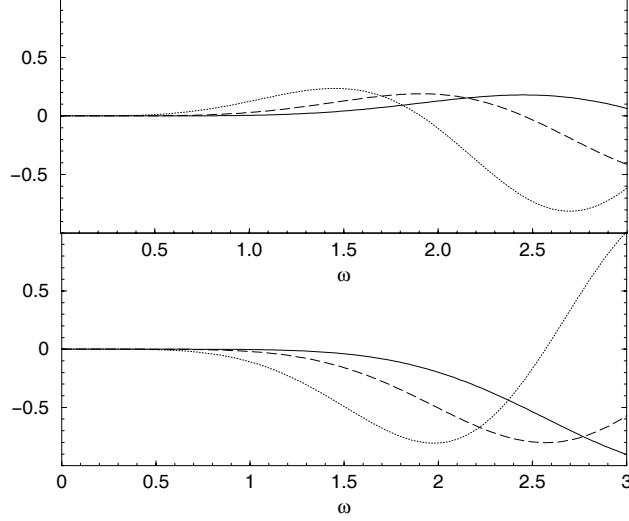
16

Figure 10: Real (upper figure) and imaginary (lower figure) parts of the Fourier transform $\hat{\psi}(\omega)$ of the univariate SDD6 mother wavelet (solid lines) and their first (dashed lines) and second (dotted lines) derivatives near the origin.

products

$$\gamma_{j,\mathbf{a}}^{(s)}(\mathbf{r})\,\gamma_{l,\mathbf{b}}^{(t)}(\mathbf{r}) = \sum_u \sum_m \sum_{\mathbf{c}} \left(\begin{array}{ccc} j & l & m \\ \mathbf{a} & \mathbf{b} & \mathbf{c} \end{array} \right) \gamma_{m,\mathbf{c}}^{(u)}(\mathbf{r}). \tag{34}$$

The properties of wavelet coupling coefficients

$$\left(\begin{array}{ccc} j & l & m \\ \mathbf{a} & \mathbf{b} & \mathbf{c} \end{array} \right) := \int d^3 r \, \gamma_{j,\mathbf{a}}^{(s)}(\mathbf{r}) \, \gamma_{l,\mathbf{b}}^{(t)}(\mathbf{r}) \, \tilde{\gamma}_{m,\mathbf{c}}^{(u)}(\mathbf{r}) \tag{35}$$

have been extensively studied in paper I. In contrast to plane waves and Gaussian-type orbitals (GTO), which are the most popular types of basis functions in electronic structure calculations, wavelets are not closed under multiplication. Instead, the sum (34) contains an infinite number of terms. It has been shown in paper I, that the decay property of wavelet coupling coefficients is related to the Sobolev regularity t of the underlying univariate wavelet basis $t := \sup\{s : \psi_{j,a} \in H^s\}$, where H^s denotes Sobolev spaces with real coefficient s. The wavelet coupling coefficients decay exponentially

$$\left| \left(\begin{array}{ccc} j & l & m \\ \mathbf{a} & \mathbf{b} & \mathbf{c} \end{array} \right) \right| \leq C(j,l)\, 2^{-t(m-\max\{j,l\})} \qquad \text{for} \quad m \geq j,l \tag{36}$$

with respect to the wavelet level m. Their fast decay offers the possibility to apply the expansion (34) to pointwise wavelet products on vertices of diagrams. At first, we have to increase the finest level of the 3d-wavelet basis from $l_{\max}$ to $l_{\max} + p$. Depending on the specific regularity of the wavelet basis, the number of additional levels p has to be chosen in such a way that the magnitudes of the coupling coefficients (35), which are not taken into account, are beyond a certain threshold. For the applications in mind, $p = 2$ or 3 should be sufficient. It has to be mentioned that wavelet coefficients are directly related to the approximation error in L^2 and H^1 norms, which means that we have a rigorous control on the accuracy of the product expansion (34) in the corresponding function spaces.

Applying the product expansion (34) to the diagrams of the recurrence scheme means, that those sets of diagrams with one or two wavelet products on their vertices can be represented in terms of wavelet coupling coefficients (35) and extended sets of diagrams with single wavelets located on the corresponding vertices. Typical examples are the sets of basic type 5 and 6 diagrams, which can be obtained from extended sets of type 3-2 and 3-1 diagrams, respectively. A major advantage of this decomposition consists in additional
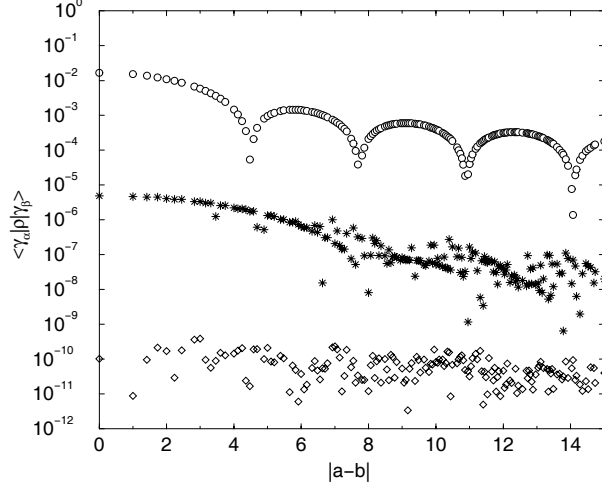
Figure 11: Wavelet representation of the density matrix $\rho(r_{12})$ of a homogeneous electron gas with Fermi momentum $k_F = 1$ bohr^{-1}. Matrix elements for three different combinations of wavelets $\gamma_{0,\mathbf{a}}^{(p)}$ and scaling functions $\beta_{0,\mathbf{a}}$ have been selected: ($\circ$) $\langle \beta_{0,\mathbf{a}} | \rho(r_{12}) | \beta_{0,\mathbf{b}} \rangle$, ($\star$) $\langle \beta_{0,\mathbf{a}} | \rho(r_{12}) | \gamma_{0,\mathbf{b}}^{(1)} \rangle$, ($\diamond$) $\langle \gamma_{0,\mathbf{a}}^{(7)} | \rho(r_{12}) | \gamma_{0,\mathbf{b}}^{(7)} \rangle$. Absolute values of these matrix elements at distance $|\mathbf{a} - \mathbf{b}|$ are plotted on a logarithmic scale. The isotropic 3d-wavelets were generated from the univariate SDD6 wavelet basis (see Appendix A).

sparsity because of the vanishing moment property, which acts on a larger number of vertices. This is of special importance for the intermediate steps of the recurrence scheme, where external lines give rise to $O(N^2)$ or $O(N^4)$ prefactors for the total computational complexity. The final reconstruction, using wavelet coupling coefficients, has to be carried out only for sets of closed diagrams. It remains to determine the cardinalities of the extended sets of diagrams. At first, intermediate sets of diagrams with only a wavelet product on their vertices are replaced by the corresponding sets of diagrams with individual wavelets on these vertices as it is shown schematically in Fig. 12, where the levels k, l of a wavelet product are indicated. The cardinality of the extended 3d-wavelet bases, represented by filled symbols in the diagrams, is $O(M)$, which has to be compared with an $O(M \log(M))$ cardinality for pointwise wavelet products. In practical calculations, however, the formal improvement is compensated by a larger constant for the extended wavelet basis. At next, we have to consider sets of intermediate diagrams with a single wavelet connected to a wavelet product. The cardinalities for these sets of diagrams and the corresponding extended sets with two single wavelets on the vertices are both $O(M^2)$, however, with the essential difference that the vanishing moment property becomes much more efficient in the latter case. Concerning the final sets of diagrams, we first have to consider the case of two single wavelets and one wavelet product on the vertices. Because of the sparse grids constraint for the wavelet tensor products, there is a correlation between the wavelet levels on the vertices. Let $Q = \tilde{Q} - 2(l_0 - 1)$ be a modified threshold parameter (6). For the level combinations depicted in Fig. 12, we obtain the constraints $k \leq Q - j$ and $l \leq Q - o$ for the levels of the pointwise wavelet product. Consequently, the product expansion (34) can be restricted to the levels $m \leq Q - \min\{j, o\} + p$. The cardinality of extended sets therefore remains $O(M^2 \log(M))$, as for the original sets of diagrams. Again, we have achieved an improved sparsity because of the vanishing moment property. Analogous arguments applied to sets of diagrams with two wavelet products on their vertices yields cardinalities of $O(M^2)$ for the extended sets of diagrams like for the original ones.

3   Numerical studies for FHNC Jastrow factors

In the previous section, we have studied the sparsity of sets of diagrams based on the vanishing moment property of the wavelet basis that has been used for the expansion of the Jastrow factor. The sparsity patterns reflect local properties within the multiresolution analysis of diagrams. In order to study global
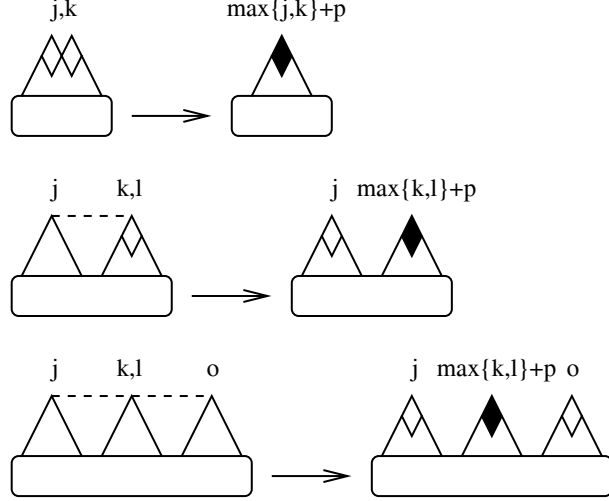
Figure 12: Wavelet expansion of pointwise wavelet products. Schematic representation of diagrams with a wavelet product on a vertex and a differing number of single wavelets on other vertices. The corresponding wavelet levels are shown on the vertices. Filled symbols represent extended 3d-wavelet basis, where the finest level of the product expansion has been indicated.

features of wavelet expansions, we have to consider the contracted pair-correlation function

$$\mathcal{F}^{(2)}(\mathbf{r}_1, \mathbf{r}_2) = \sum_\Lambda f_\Lambda \, \mathcal{F}_\Lambda(\mathbf{r}_1, \mathbf{r}_2) \tag{37}$$

of a Jastrow factor, cf. Eq. (4). The corresponding global diagrams for contracted pair-correlation functions can be obtained as bilinear forms

$$\mathcal{D}_n[\mathcal{F}^{(2)}, \mathcal{F}^{(2)}] = \sum_{\Lambda,\Omega} \mathcal{D}_n[\mathcal{F}^{(2)}_\Lambda, \mathcal{F}^{(2)}_\Omega] \, f_\Lambda \, f_\Omega, \tag{38}$$

where the coefficients $\mathcal{D}_n[\mathcal{F}_\Lambda, \mathcal{F}_\Omega]$ denote individual elements from the set of type n diagrams. Within the local ansatz, there is no necessity to calculate these global diagrams because of Eq. (14) for the correlation energy. Nevertheless, global diagrams are useful tools to study the convergence behaviour of wavelet expansions with respect to the energy if one is not willing to solve the full many-body problem. Before the development of self-consistent optimization schemes, like the FHNC method, it was common practice in nuclear physics to study cluster expansions of the energy [31] for a given Jastrow factor. Such kind of cluster expansions provide useful insight into the significance of various types of diagrams with respect to the energy [51, 55]. For our present purposes it is sufficient to take a wavelet expansion of a Jastrow factor that has been optimized by some other method. More important than the details of the Jastrow factor is an appropriate choice of the model system.

According to our previous discussion it is obvious that the sparsity of certain sets of diagrams depend to a large extend on the oscillatory behaviour of the density matrix. Therefore, we have taken the homogeneous electron gas as a reference system, where the strength of oscillations is determined by a single parameter, namely the Fermi momentum k_F. We have used the standard supercell approach with periodic boundary conditions [56]. The Coulomb potential has been replaced by an Ewald potential in order to take properly into account electron-electron interactions between the central supercell and its periodic images. Although, the homogeneous electron gas is a convenient model from the computational point of view, we have to mention that due to the presence of long-range correlations, the local ansatz is not really appropriate. Long-range correlations cause certain types of diagrams, like the ring diagram 1-3-1-2, to diverge in the thermodynamic limit. Subtle Fermi cancellation phenomena [31] with respect to

higher order diagrams are required to get rid of these divergences. The local ansatz does not incorporate contributions beyond second order, which leads to a wrong long-range behaviour of the Jastrow factor. It requires a nonlinear approach like the FHNC method to get a proper description of long-range correlations. We have therefore neglected the long-range contributions to the Jastrow factor and concentrate on the short and intermediate regime.

In our numerical studies, we consider only diagrams emerging from basic type 1 or 4 diagrams, where wavelets are located on at most one vertex of the Coulomb interaction. The Fourier representation of the Ewald potential

$$U_{\text{Ewald}}(\mathbf{r}_i, \mathbf{r}_j) = \frac{4\pi}{V_{SZ}} \sum_{\mathbf{k} \neq 0} \frac{e^{-i\mathbf{k}(\mathbf{r}_i - \mathbf{r}_j)}}{|\mathbf{k}|^2} \tag{39}$$

is appropriate for such kind of diagrams, because the Fourier series terminates after a finite number of terms. For our calculations, we have chosen an electron density of $r_s = 2.07$ ($k_F = 0.927$ bohr^{-1}). This corresponds to the average valence electron density in aluminium. The cubic supercell with edge length 12 bohr contains 54 electrons. An almost optimal Jastrow factor with correct long-range behaviour has been obtained from a FHNC//0 calculation [46]. Within the supercell approach, such kind of Jastrow factor requires an Ewald summation for the long-range part [56]. In order to avoid this additional complication, and in view of the inappropriate treatment of long-range correlations within the local ansatz discussed above, we have introduced an appropriate cutoff procedure. The FHNC pair-correlation function can be efficiently approximated by a linear combination of Gaussian-type geminals [57]

$$\mathcal{F}_{\text{FHNC}}^{(2)}(\mathbf{r}_1, \mathbf{r}_2) = \sum_i c_i \, e^{-\alpha_i (\mathbf{r}_1 - \mathbf{r}_2)^2}, \tag{40}$$

where the parameters c_i, α_i have been optimized within the distance range $|\mathbf{r}_1 - \mathbf{r}_2| \leq r_{\max}$. In our present application we have chosen $r_{\max} = 16$ bohr. Up to this distance, the expansion (40) provides an accurate approximation of the FHNC//0 Jastrow factor, except at very small distances $|\mathbf{r}_1 - \mathbf{r}_2| \leq r_{\min}$ close to the inter-electron cusp. We have included sufficiently large exponents α_i in order to make sure that $r_{\min} \ll 2^{-j_{max}}$, where j_{max} is the finest level that has been taken into account for the wavelet expansion of the Jastrow factor. Therefore this discrepancy does not affect our results since it appears on a length scale that cannot be resolved by wavelets on levels $j \leq j_{max}$ anyhow. At large distances $|\mathbf{r}_1 - \mathbf{r}_2| > r_{\max}$, the expansion (40) provides a smooth exponential cutoff, that allows for a direct summation of the images of the central supercell. A further advantage of the approximation (40) is that we can calculate analytically the "exact" values of the diagrams under consideration, which are required for a discussion of the approximation error of the wavelet expansion.

Before entering into a quantitative discussion of convergence properties for wavelet expansions, we want to illustrate the sparsity features for diagrams with L-1 type vertices. In Fig. 13 a), we have shown the absolute magnitude of elements in the set of type 1-7 diagrams. The maximum value, with respect to the set of orbital indices for the two external lines, has been taken for each diagram. For coarse wavelet levels, a typical sparsity pattern can be observed, where the dominant contributions are concentrated near the origin and along the axes. Such kind of sparsity pattern indicates that hyperbolic tensor products dominate the set of type 1-7 diagrams. Contributions from finer wavelet levels are almost negligible in agreement with our previous discussion of the density matrix for a homogeneous electron gas. It is interesting to compare the sparsity pattern of the diagrams 1-7 with the sparsity pattern of the Jastrow factor, which is shown in Fig. 13 b). Due to asymptotic smoothness of the Jastrow factor, the sparsity pattern is more pronounced and shows a similar concentration at the origin and along the axes. Furthermore, the inter-electron cusp gives rise to a distinct diagonal dominance at the finer wavelet levels.

Among the descendents of the set of basic type 1 diagrams, we focused on the global diagrams 1-3-1-2, 1-6-2 and 1-7-1, where the first and third diagram belongs to the class of ring and ladder diagrams, respectively. The convergence behaviour for these diagrams with respect to hyperbolic wavelet expansions of the Jastrow factor is shown in Fig. 14. Relative errors versus the number of hyperbolic 3d-wavelet
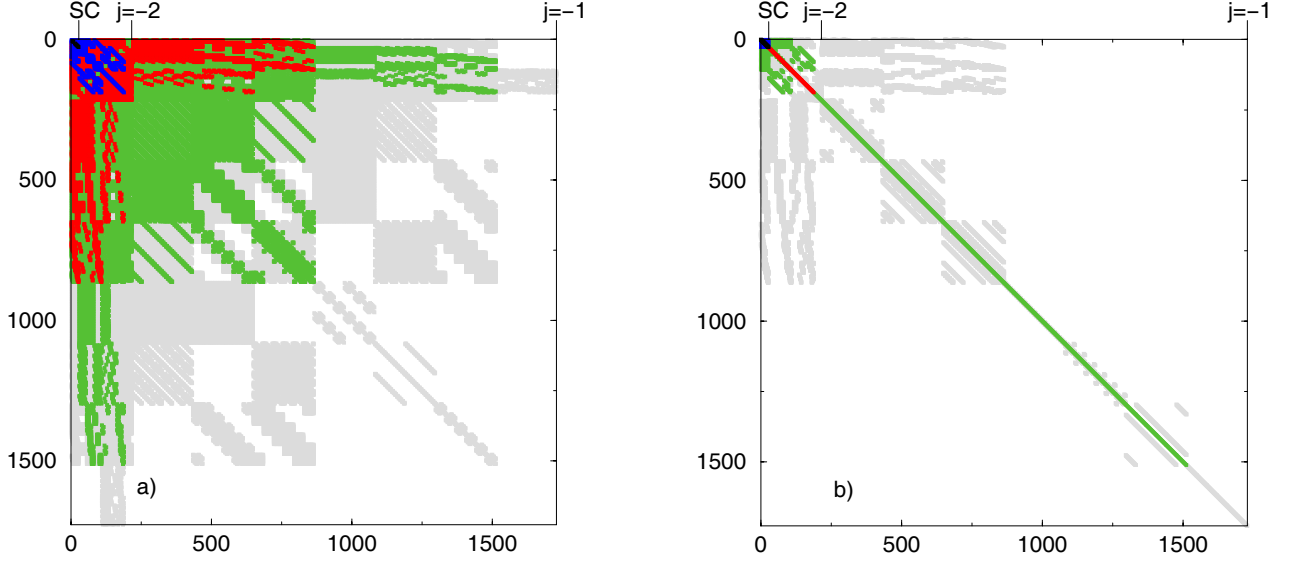
Figure 13: Sparsity patterns of isotropic 3d-wavelet tensor products for a homogeneous electron gas at $r_s = 2.07$. a) Set of type 1-7 diagrams. b) FHNC//0 Jastrow factor. The isotropic 3d-wavelets are numbered consecutively with increasing level. Absolute values of scaling function (SC) and wavelet tensor product coefficients on levels $j = -2$ and $j = -1$ are represented by different gray shades. In white regions the absolute values are below 10^{-4}. Starting with the lightest gray tone at 10^{-4}, the absolute values increase by a factor of 10 with each shade. The isotropic 3d-wavelets have been obtained from SDD6 univariate wavelets. Translational symmetry has been only taken into account with respect to the coarsest wavelet level $l_0 = -2$ in the tensor products.

tensor products are shown with and without diagonal refinement. At each level of refinement, we have also indicated the sparse grids parameter $\tilde{Q}$. It can be seen that the overall convergence for these three types of diagrams is rather similar. Diagonal refinement improves the results considerably in almost all cases with low additional costs. A remarkable exception appears for $\tilde{Q} = 2$, where diagonal refinement seemingly provides almost no improvements. This is due to the fact that our selection scheme only reflects the significance of wavelet tensor products with respect to an approximation of the Jastrow factor itself. In the case of a diagram, where the effect of the vanishing moments on the density matrices has to be taken into account, the situation can be more complex. A closer look at the approximation errors reveals that diagonal refinement provides exactly the same improvement for $\tilde{Q} = 2$ and $\tilde{Q} = 3$, which, however, is obscured by the logarithmic scale. On levels $\tilde{Q} = 2, 3$, the dominant contribution to diagonal refinement consists of tensor products where both wavelets are on level $j = -1$. Without diagonal refinement, these tensor products appear for the first time at $\tilde{Q} = 4$. The overall effect of these tensor products, however, is rather small for these diagrams, due to their interaction with the density matrices, as can be seen from Fig. 13 a). For comparison, we have also considered the global diagram 4-2-2, which has a wavelet product on a vertex of the Coulomb interaction. It can be seen from Fig. 14, that the overall convergence for this diagram is rather similar to the previous ones. Just a slight increase of the relative errors on the various levels has been observed. This is a consequence of the reduced number of vertices, where vanishing moments suppress contributions from wavelets on finer scales. Such kind of observations can be extended to a large class of diagrams, which means that for these diagrams fairly high accuracies can be achieved already on relatively coarse levels of the hyperbolic wavelet expansion. Large contributions from fine wavelet levels can be expected for example in the case of diagrams like 1-1-6, 1-1-2-1, 1-4-1 etc., where pair-correlation functions run parallel to each other or to the Coulomb interaction.

Besides hyperbolic wavelet expansions for isotropic 3d-wavelets, we have also tested fully anisotropic expansions based on anisotropic 3d-wavelets, where we refer to Appendix A for further details. An
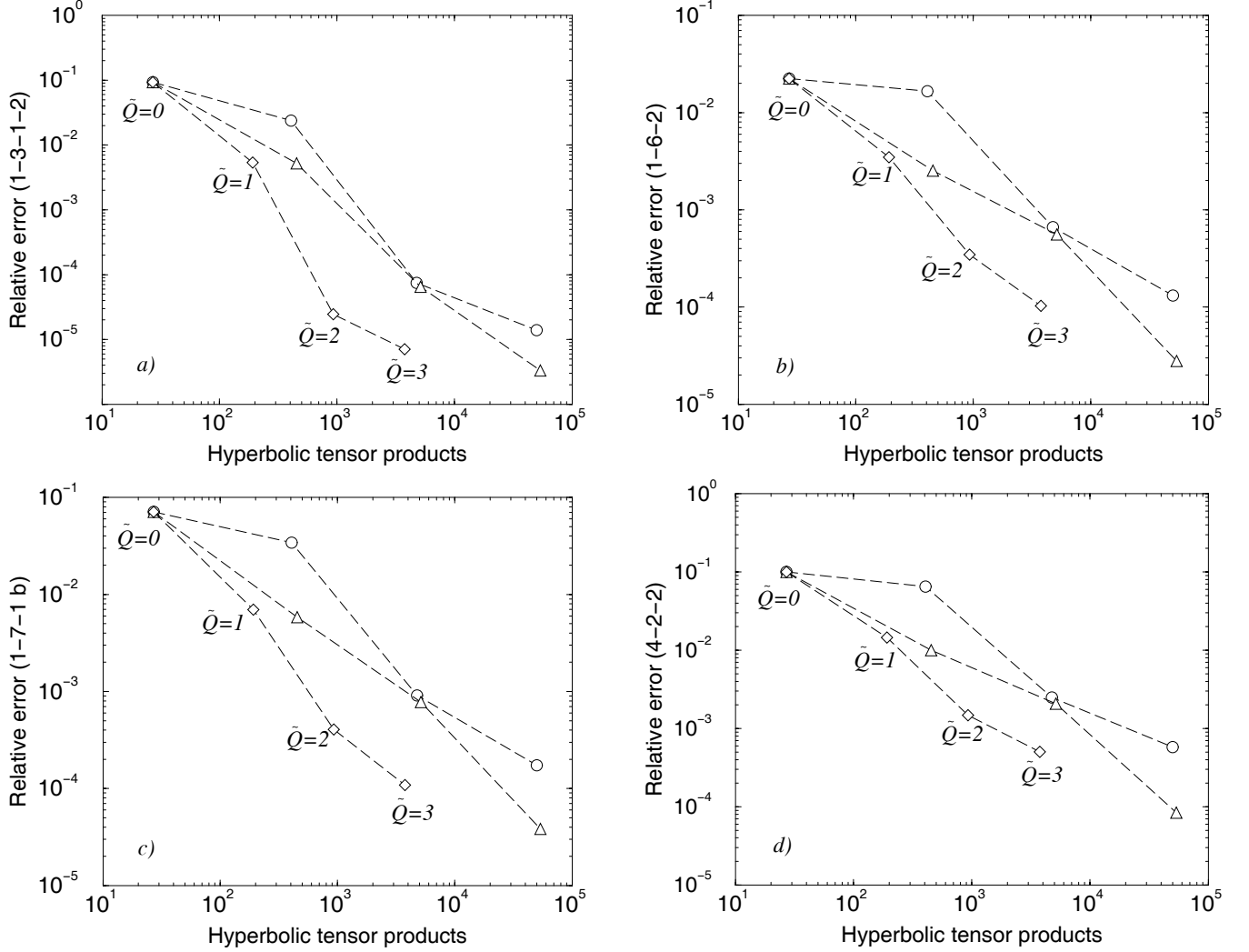
21

Figure 14: Convergence of selected diagrams for hyperbolic wavelet expansions of a FHNC//0 pair-correlation function in the case of a homogeneous electron gas at $r_s = 2.07$. Relative errors versus the number of hyperbolic wavelet tensor products are shown for the diagrams a) 1-3-1-2 (ring diagram), b) 1-6-2, c) 1-7-1 b (ladder diagram), d) 4-2-2. Three different types of hyperbolic tensor products have been employed: Isotropic ($\triangle$) and anisotropic ($\diamond$) 3d-wavelets with diagonal refinement as well as without diagonal refinement in the isotropic case ($\circ$). Isotropic and anisotropic 3d-wavelets have been obtained from the univariate SDD6 wavelet basis. Translational symmetry has been only taken into account with respect to the coarsest wavelet level $l_0 = -2$ in the expansion.

22

advantage of the latter is, that the sparse grid constraint acts on all six dimensions. This reduces the cardinality of the set of hyperbolic tensor products from $O(M \log(M))$ to $O(m \log(m)^5)$, where m is the cardinality of the univariate wavelet basis. In view of the relation $M \sim m^3$ between the cardinalities of isotropic 3d-wavelets and the underlying univariate wavelet basis, this is a considerable reduction of the computational complexity. A drawback of this approach is that because of the highly anisotropic character of these tensor products, the analysis of the computational complexity for diagrams is considerably more complicated. For the same reason, there is no obvious adaptive refinement scheme at the inter-electron cusp. We have tried a scheme, outlined in Appendix A, which is a straightforward extension of the isotropic case. Results for the fully anisotropic expansions are shown in Fig. 14, where we observed almost the same convergence behaviour with respect to $\tilde{Q}$ as for the isotropic case, however, with a considerably smaller number of wavelet tensor products. It requires further investigations to see whether this observation can be confirmed for diagrams with larger contributions from the inter-electron cusp.

4   Summary and conclusions

We have presented a general framework for a wavelet based multiresolution analysis of electron correlations. It is based on a product ansatz for the wavefunction, where we take Jastrow-type correlation functions for the description of electron correlations. Sparse wavelet expansions with almost linear complexity exist, due to the asymptotic smoothness of Jastrow factors. Their sparsity patterns correspond to hyperbolic tensor products with additional diagonal refinement because of the inter-electron cusp. There are good physical reasons to extend this ansatz to more general types of correlation operators, which have already proved useful in solid state physics [49]. In order to be of practical significance, multiresolution analysis requires efficient and accurate many-particle methods, which are compatible with the peculiar features of wavelet bases. A linear expansion of Jastrow factors enables a strictly variational optimization of the wavefunction. However, in order to achieve a constant relative accuracy for extended systems, the sparse grids parameter $\tilde{Q}$ has to be adapted to the the size of the system in order to satisfy the size-consistency requirement. Such kind of truncation scheme becomes impracticable for extended systems, because of a strong increase of computational complexity with the size of the system. To get rid of this problem, we have taken an exponential ansatz for the Jastrow factor, where the wavelet expansion has been restricted to pair-correlation functions. The resulting nonlinear optimization problem has been linearized by using the local ansatz of Stollhoff and Fulde, which provides a flexible and size-consistent many-particle scheme. Neglecting systematic errors inherent to the local ansatz, we have studied interrelations between the level of resolution and computational complexity for electron correlations. Within the present work no restrictions concerning the decay properties of one-particle density matrices have been imposed.

Straightforward application of diagrammatic techniques enables a formal evaluation of matrix elements for the local ansatz. The FHNC like diagrams can be represented in terms of one-particle density matrices, the Coulomb interaction and pair-correlation functions consisting of hyperbolic wavelet tensor products. We have studied the computational complexity for the evaluation of these diagrams and derived a recurrence scheme, which is based on sets of certain types of basic Coulomb and chain diagrams. The central topic of the present work are specific sparsity features of these diagrams, which are due to the hierarchical character and the vanishing moment property of wavelet bases. It has been shown that the computational complexity increases almost quadratically with respect to the size of the underlying 3d-wavelet basis. Introducing wavelet expansions of pointwise wavelet products on the vertices of the diagrams introduces further sparsity, which might led to almost linear complexity at least for the intermediate sets of diagrams in the recurrence scheme. These sets are crucial from a computational point of view because their cardinalities strongly depend on the number of electrons in the system. This is due to the presence of external orbitals lines in the corresponding diagrams.

The diagrammatic multiresolution analysis introduced within the present work is still in its infancy. We were faced with technical limitations concerning the types of diagrams that can be handled for a homogeneous electron gas. In a subsequent publication, we want to discuss a complete integration scheme

for the Ewald potential, which can be applied to all types of basic Coulomb diagrams. We plan in our future work, to study in more detail the actual contributions of specific scales for certain types of diagrams as well as the couplings between different scales. Better estimates are required in order to decide which sets of diagrams give the dominant contributions on specific length- and energy-scales.

5 Acknowledgments

Appendices

A Multiresolution analysis in higher dimensions

The purpose of this appendix is to provide some basic definitions and properties of wavelets which are required for this paper. For a complete exposition of this subject, we refer to the excellent monographs of Daubechies [2] and Mallat [5]. In particular we define various types of wavelet basis in higher dimensions. From the computational point of view, tensor product constructions are the simplest and most flexible approach. Higher dimensional wavelets are constructed successively by taking appropriate tensor products of an univariate wavelet basis.

In one dimension, multiresolution analysis provides a partition of the Hilbert space $L^2(\mathbb{R})$ into an infinite sequence of ascending subspaces $\cdots \subset V_{j-1} \subset V_j \subset V_{j+1} \subset \cdots$, where the index j runs over all integers. The union of these subspaces $\bigcup_j V_j$ is dense in $L^2(\mathbb{R})$. On each subspace V_j, the scaling function $\varphi(x)$ provides a basis

$$\varphi_{j,a}(x) := 2^{j/2} \varphi(2^j x - a), \tag{41}$$

via the operations of dilation and translation. The dilation factor 2^j scales the size of the basis functions, which means that with increasing j, the $\varphi_{j,a}$ provide a finer resolution in L^2. An explicit embedding of V_j into the larger space V_{j+1} is given by the refinement relation

$$\varphi(x) = 2 \sum_a h_a \, \varphi(2x - a), \tag{42}$$

where the number of nonzero filter coefficients h_a is finite for the scaling functions used in our applications. Wavelet spaces W_j are defined as complements of V_j in V_{j+1}. The corresponding wavelet basis is generated from a mother wavelet $\psi(x)$ analogous to Eq. (41)

$$\psi_{j,a}(x) := 2^{j/2} \psi(2^j x - a). \tag{43}$$

This construction leads to a hierarchical decomposition of $L^2 = \bigoplus_{j \in \mathbb{Z}} W_j$ into wavelet subspaces W_j [2]. In a biorthogonal wavelet basis there exists a sequence of dual spaces $\tilde{V}_j$, $\tilde{W}_j$, which satisfy the orthogonality relations $\tilde{W}_j \perp V_j$ and $\tilde{V}_j \perp W_j$. The corresponding dual wavelets $\tilde{\psi}_{j,a} := 2^{j/2} \tilde{\psi}(2^j x - a)$ and scaling functions $\tilde{\varphi}_{j,a} := 2^{j/2} \tilde{\varphi}(2^j x - a)$ provide a biorthogonal basis in L^2

$$\langle \varphi_{j,a} | \tilde{\varphi}_{j,b} \rangle = \delta_{a,b}, \qquad \langle \psi_{j,a} | \tilde{\psi}_{l,b} \rangle = \delta_{j,l} \, \delta_{a,b}. \tag{44}$$

An arbitrary function in $L^2(\mathbb{R})$ can be expanded in a biorthogonal wavelet basis

$$f(x) = \underbrace{\sum_a \langle \tilde{\varphi}_{l_0,a} | f \rangle \, \varphi_{l_0,a}(x)}_{V_{l_0}} + \underbrace{\sum_{j=l_0}^{\infty} \sum_a \langle \tilde{\psi}_{j,a} | f \rangle \, \psi_{j,a}(x)}_{\bigoplus_{l_0 \le j} W_j}, \tag{45}$$

where the scaling function and wavelet coefficients are given by scalar products with respect to the dual basis. The multiscale approximation of smooth functions reveals an important sparsity feature due to the vanishing moments property of wavelets. Depending on the specific choice of the wavelet basis, a certain number of moments vanish

$$\int dx \, x^k \, \tilde{\psi}(x) = 0, \text{ for } k = 0, \ldots, n-1. \tag{46}$$

This property has a significant effect on the magnitude of wavelet coefficients, as can be seen from local Taylor series expansions

$$f(x) = c_0 + \cdots + c_{n-1}(x - 2^{-j}a)^{n-1} + R_{n-1}(x)(x - 2^{-j}a)^n, \tag{47}$$

around the centers of wavelets $\tilde{\psi}_{j,a}(x)$. Inserting the Taylor series expansions (47) into the scalar products yields the following estimate for the wavelet coefficients

$$|v_{j,a}| = \left| \int dx \, f(x) \, \tilde{\psi}_{j,a}(x) \right| \leq \sup_{\text{supp}\{\tilde{\psi}_{j,a}\}} |R_{n-1}(x)| \, 2^{-j(n+1/2)} \int dx \, \left| x^n \tilde{\psi}(x) \right|, \tag{48}$$

where the supremum of the remainder $|R_{n-1}(x)|$ has to be taken with respect to the support of wavelets $\tilde{\psi}_{j,a}(x)$. For functions with rapidly converging local Taylor series, the corresponding wavelet expansions (45), therefore, converge very fast with respect to the level j. This leads to sparse wavelet representations for these functions. Such kind of arguments can be extended to singular kernel functions [9, 10, 11, 12], which satisfy the asymptotic smoothness condition (25). For our numerical studies, we have used the univariate biorthogonal wavelets with six vanishing moments of Sweldens [58] and the corresponding univariate scaling function of Deslauriers and Dubuc [59]. In the text, we refer to this basis as the SDD6 wavelet basis.

Isotropic 3d-wavelets are constructed by taking mixed tensor products of wavelets $\psi_{j,a}$ and scaling functions $\varphi_{j,a}$ on the same level j

$$\begin{aligned}
\beta_{j,\mathbf{a}}(\mathbf{r}) &= \varphi_{j,a_x}(x) \, \varphi_{j,a_y}(y) \, \varphi_{j,a_z}(z), \\
\gamma_{j,\mathbf{a}}^{(1)}(\mathbf{r}) &= \psi_{j,a_x}(x) \, \varphi_{j,a_y}(y) \, \varphi_{j,a_z}(z), \\
&\vdots \\
\gamma_{j,\mathbf{a}}^{(4)}(\mathbf{r}) &= \psi_{j,a_x}(x) \, \psi_{j,a_y}(y) \, \varphi_{j,a_z}(z), \\
&\vdots \\
\gamma_{j,\mathbf{a}}^{(7)}(\mathbf{r}) &= \psi_{j,a_x}(x) \, \psi_{j,a_y}(y) \, \psi_{j,a_z}(z).
\end{aligned} \tag{49}$$

These multivariate wavelets belong to well defined levels j, however, there are seven different types of them, according to the different combinations of univariate wavelets and scaling functions. Sometimes it is convenient to use the notation $\gamma_{j,\mathbf{a}}^{(0)} := \beta_{j,\mathbf{a}}$ for the 3d-scaling functions and an analogous notation $\psi_{j,a}^{(0)}(x) := \varphi_{j,a}(x), \psi_{j,a}^{(1)}(x) := \psi_{j,a}(x)$ for the univariate case.

An alternative approach to multivariate wavelets are standard tensor products in the hierarchical univariate wavelet basis

$$\begin{aligned}
\chi_{\mathbf{j},\mathbf{a}}(\mathbf{r}) &= \psi_{j_x,a_x}(x) \, \varphi_{l_0,a_y}(y) \, \varphi_{l_0,a_z}(z), \text{ with } \mathbf{j} := (j_x, l_0 - 1, l_0 - 1), \\
&\vdots \\
\chi_{\mathbf{j},\mathbf{a}}(\mathbf{r}) &= \psi_{j_x,a_x}(x) \, \psi_{j_y,a_y}(y) \, \varphi_{l_0,a_z}(z), \text{ with } \mathbf{j} := (j_x, j_y, l_0 - 1), \\
&\vdots \\
\chi_{\mathbf{j},\mathbf{a}}(\mathbf{r}) &= \psi_{j_x,a_x}(x) \, \psi_{j_y,a_y}(y) \, \psi_{j_z,a_z}(z), \text{ with } \mathbf{j} := (j_x, j_y, j_z),
\end{aligned} \tag{50}$$

where different wavelet levels can appear in the various directions. Within an anisotropic 3d-wavelet basis, only scaling functions on the coarsest level l_0 show up in the tensor products. The different wavelet levels in the tensor products are characterized by the multilevel index $\mathbf{j}$, where for scaling functions the level index is $l_0 - 1$. We have employed isotropic and anisotropic 3d-wavelets for the expansion of the Jastrow factor.

Isotropic and anisotropic wavelet constructions become impracticable beyond three dimensions. For the expansion of the Jastrow factor, we, therefore, have to switch to hyperbolic wavelets [32]. The concept of hyperbolic wavelets is based on a special kind of hierarchical ordering and truncation scheme for standard tensor products of isotropic

$$\gamma_{j_1,\mathbf{a}_1}^{(s_1)}(\mathbf{r}_1)\,\gamma_{j_2,\mathbf{a}_2}^{(s_2)}(\mathbf{r}_2)\ldots\gamma_{j_p,\mathbf{a}_p}^{(s_p)}(\mathbf{r}_p), \tag{51}$$

or anisotropic

$$\chi_{\mathbf{j}_1,\mathbf{a}_1}(\mathbf{r}_1)\,\chi_{\mathbf{j}_2,\mathbf{a}_2}(\mathbf{r}_2)\ldots\chi_{\mathbf{j}_p,\mathbf{a}_p}(\mathbf{r}_p) \tag{52}$$

3d-wavelets, respectively. Due to their anisotropic character, we cannot assign a unique level to these tensor products. Instead, we have to take their level sums in order to get a hierarchical ordering. For tensor products of isotropic 3d-wavelets, the level sum $|\mathbf{J}|$ is given in Eq. (6). Correspondingly, for tensor products of anisotropic 3d-wavelets (52), the level sum is defined as

$$|\mathbf{J}| := \sum_{i=1}^{p}\left(|\mathbf{j}| - 3l_0 + 3\right), \quad \text{with} \quad |\mathbf{j}| := j_x + j_y + j_z, \tag{53}$$

where p is the number of 3d-wavelets in the tensor product (52). A hierarchical ordering of the hyperbolic wavelet expansion is now introduced via the sparse grid parameter $\tilde{Q}$, which imposes the constraint $|\mathbf{J}| \leq \tilde{Q}$ on the tensor products. The cardinalities of the corresponding tensor product bases increase with $O(2^{3\tilde{Q}}\tilde{Q}^{p-1})$ and $O(2^{\tilde{Q}}\tilde{Q}^{3p-1})$ for isotropic and anisotropic 3d-wavelets, respectively. In the case of anisotropic 3d-wavelets, there is no obvious scheme for diagonal refinement at the inter-electron cusp. We have tried an ad hoc procedure, formally analogous to the isotropic case, where we allow for all tensor products $\chi_{\mathbf{j},\mathbf{a}}(\mathbf{r}_1)\chi_{\mathbf{j},\mathbf{a}}(\mathbf{r}_2)$ with $|\mathbf{j}| \leq \tilde{Q}$ irrespective of their level sum (53). Hyperbolic tensor products are well known in finite element methods as sparse grids [60, 61, 62]. First applications of sparse grids in electronic structure calculations by Garcke and Griebel [63] demonstrate the usefulness of this method. Recently, the sparse grids method has been further improved by introducing the concept of dimension-adaptive tensor products [64, 65].

B   Contraction rules for biorthogonal wavelet bases

In order to apply second quantization and Wick's theorem for operators represented in a biorthogonal wavelet basis, a few technical points need to be clarified. The modifications required in this case are straightforward and have been routinely applied in the literature [43]. For formal reasons, we introduce an orthogonal one-particle basis ϕ_i, $i = 1,\ldots,\infty$, which is supposed to be complete in $L^2(\mathbb{R}^3)$. In the following we refer to this basis as the orbital basis. The first N basis functions correspond to occupied HF spin-orbitals of the system under consideration. For notational convenience, in the orbital basis indices $a, b, \ldots$ run over occupied orbitals and $r, s, \ldots$ run over virtual orbitals, whereas indices $i, j, \ldots$ run over the whole basis. It has to be mentioned that an explicit knowledge beyond the first N basis functions is not required in the following. In order to apply Wick's theorem for the evaluation of matrix elements [52], we have to determine contractions between pairs of operators. As usual normal ordering is defined with respect to the HF reference wavefunction, which corresponds to the "vacuum" state in this formalism. According to these definitions, contractions within the orbital basis are given by

$$\overset{\frown}{\hat{\phi}_a\hat{\phi}_i^\dagger} = \overset{\frown}{\hat{\phi}_r^\dagger\hat{\phi}_i} = \overset{\frown}{\hat{\phi}_i^\dagger\hat{\phi}_j^\dagger} = \overset{\frown}{\hat{\phi}_i\hat{\phi}_j} = 0, \qquad \overset{\frown}{\hat{\phi}_a^\dagger\hat{\phi}_b} = \delta_{a,b}, \qquad \overset{\frown}{\hat{\phi}_r\hat{\phi}_s^\dagger} = \delta_{r,s}. \tag{54}$$

The wavelet basis γ_α can be represented in the orbital basis

$$\gamma_\alpha(\mathbf{r}, \sigma) = \sum_i c_{\alpha,i}\, \phi_i(\mathbf{r}, \sigma), \text{ with } c_{\alpha,i} = \langle \phi_i | \gamma_\alpha \rangle, \tag{55}$$

which yields the following representation for creation and annihilation operators in the wavelet basis

$$\hat{\gamma}_\alpha^\dagger = \sum_i c_{\alpha,i}\, \hat{\phi}_i^\dagger \qquad \hat{\gamma}_\alpha = \sum_i c_{\alpha,i}^*\, \hat{\phi}_i. \tag{56}$$

The corresponding anticommutation relations are given by

$$\left[\hat{\gamma}_\alpha^\dagger, \hat{\gamma}_\beta\right] = \langle \gamma_\alpha | \gamma_\beta \rangle, \qquad [\hat{\gamma}_\alpha, \hat{\gamma}_\beta] = 0, \qquad \left[\hat{\gamma}_\alpha^\dagger, \hat{\gamma}_\beta^\dagger\right] = 0. \tag{57}$$

Straightforward application of Eqs. (54) and (55), together with the resolution of the identity $\mathbb{I} = \sum_i |\phi_i\rangle\langle\phi_i|$ yields the corresponding contractions for the wavelet creation and annihilation operators

$$\overset{\frown}{\hat{\gamma}_\alpha^\dagger \hat{\gamma}_\beta^\dagger} = \overset{\frown}{\hat{\gamma}_\alpha \hat{\gamma}_\beta} = 0, \qquad \overset{\frown}{\hat{\gamma}_\beta \hat{\gamma}_\alpha^\dagger} = \langle \gamma_\beta | \gamma_\alpha \rangle - \langle \gamma_\beta | \hat{\rho} | \gamma_\alpha \rangle, \qquad \overset{\frown}{\hat{\gamma}_\alpha^\dagger \hat{\gamma}_\beta} = \langle \gamma_\beta | \hat{\rho} | \gamma_\alpha \rangle. \tag{58}$$

The contractions are expressed through wavelet matrix elements of the HF density matrix operator $\hat{\rho} = \sum_b |\phi_b\rangle\langle\phi_b|$.

C   Cardinalities of certain types of products for isotropic 3d-wavelets

The purpose of this appendix is to provide some supplementary material which has been omitted in Section 2.1 in favour of a concise presentation. In order to estimate cardinalities for the sets of wavelet products listed in Table 1, we first consider a simplified problem and afterwards discuss the necessary modifications for a wavelet basis. Within this simplified setting, we subdivide the unit cube into a hierarchical sequence of subcubes. On the first level the unit cube is subdivided into eight subcubes with volume 2^{-3} and on the second level each of them is again subdivided into eight subcubes with volume 2^{-6}. This process continues until the l'th level has been reached. Subcubes which belong to the same level do not overlap. To each subcube, we assign a characteristic function $\xi_{j,\mathbf{a}}(\mathbf{r})$, where the indices $j, \mathbf{a}$ specify its level and location, respectively. According to our definitions, the set of characteristic functions has cardinality

$$L := \text{card}\{\xi_{m,\mathbf{a}}(\mathbf{r})\} = \frac{1}{7}\left(8 \cdot 2^{3l} - 1\right). \tag{59}$$

The cardinality of the set of nonvanishing products between characteristic functions is given by

$$\begin{aligned}
\text{card}\{\xi_{m,\mathbf{a}}(\mathbf{r})\,\xi_{n,\mathbf{b}}(\mathbf{r})\} &= \sum_{m=0}^{l} 2^{3m} \sum_{n=m}^{l} 2^{3(n-m)} \\
&= \frac{1}{7^2}\left[(56\,l + 48)\,2^{3l} + 1\right] \\
&\sim O\left(L\log(L)\right),
\end{aligned} \tag{60}$$

where the factor 2^{3j} corresponds to the number of subcubes on level j. This has to be multiplied by the number of subcubes on levels $j \le m \le l$, which overlap with an individual subcube on level j. Next, we introduce a "hyperbolic" tensor product for characteristic functions

$$\Xi_{m\mathbf{a},n\mathbf{b}}(\mathbf{r}_1, \mathbf{r}_2) := \xi_{m,\mathbf{a}}(\mathbf{r}_1)\,\xi_{n,\mathbf{b}}(\mathbf{r}_2) \qquad \text{with } m + n \le l. \tag{61}$$

The set of "hyperbolic" tensor products has cardinality

$$
\begin{aligned}
\text{card} \{\Xi_{m\mathbf{a},n\mathbf{b}}(\mathbf{r}_1,\mathbf{r}_2)\} &= \sum_{j=0}^{l}(j+1)\,2^{3j} \\
&= \frac{1}{7^2}\left[(56\,l+48)\,2^{3l}+1\right] \qquad (62)\\
&\sim O\left(L\log(L)\right),
\end{aligned}
$$

where the index j runs over all accessible sums of levels $m+n$. For each j there are $j+1$ pairs m,n satisfying $j=m+n$ and for every pair there are 2^{3j} tensor products. It can be seen that for our model, the cardinalities of the sets of pointwise products with nonvanishing overlap and of the "hyperbolic" tensor products are equal. Continuing along this line, we consider the pointwise products of characteristic functions with "hyperbolic" tensor products, where the cardinality of the corresponding set is given by

$$
\begin{aligned}
\text{card} \{\xi_{p,\mathbf{a}}(\mathbf{r}_1)\,\Xi_{m\mathbf{b},n\mathbf{c}}(\mathbf{r}_1,\mathbf{r}_2)\} &= \sum_{j=0}^{l}2^{3j}\sum_{m=0}^{j}\left[\frac{1}{7}\left(2^{3(l-m+1)}-1\right)+m\right]\\
&= \frac{1}{7^3}\left[512\cdot2^{6l}+\left(196\,l^2+28\,l-160\right)2^{3l}-9\right] \qquad (63)\\
&\sim O\left(L^2\right).
\end{aligned}
$$

Like in the previous case, index j runs over the sums of levels $m+n$. On a particular level m, the term in square brackets corresponds to the number of subcubes, which overlap with a subcube on level m including the coarser levels. It is interesting to compare with the cardinality of the set of threefold products of characteristic functions

$$
\begin{aligned}
\text{card} \{\xi_{m,\mathbf{a}}(\mathbf{r}_1)\,\xi_{n,\mathbf{b}}(\mathbf{r}_1)\,\xi_{p,\mathbf{c}}(\mathbf{r}_2)|_{\mathbf{r}_1=\mathbf{r}_2}\} &= \sum_{m=0}^{l}2^{3m}\sum_{n=m}^{l}2^{3(n-m)}\left[\frac{1}{7}\left(2^{3(l-n+1)}-1\right)+n\right]\\
&= \frac{1}{7^3}\left[\left(588\,l^2+812\,l+360\right)2^{3l}-17\right] \qquad (64)\\
&\sim O\left(L\log(L)^2\right),
\end{aligned}
$$

which are nonvanishing on the diagonal $\mathbf{r}_1=\mathbf{r}_2$. This set contains the nonseparable part of the set (63), with respect to the Coulomb interaction. Finally we consider the remaining case of pointwise products of "hyperbolic" tensor products. The cardinality of this set is given by

$$
\begin{aligned}
\text{card} \{\Xi_{m\mathbf{a},n\mathbf{b}}(\mathbf{r}_1,\mathbf{r}_2)\,\Xi_{p\mathbf{c},q\mathbf{d}}(\mathbf{r}_2,\mathbf{r}_3)\} &= \sum_{j=0}^{l}2^{3j}\sum_{n=0}^{j}\sum_{p=0}^{l}2^{3\max\{p-n,0\}}\frac{1}{7}\left(2^{3(l-p+1)}-1\right)\\
&= \frac{1}{7^4}\left[(7168\,l+1536)\,2^{6l}-\left(392\,l^2+168\,l-856\right)2^{3l}+9\right] \quad (65)\\
&\sim O\left(L^2\log(L)\right).
\end{aligned}
$$

Every characteristic function on level n has nonvanishing overlap with $2^{3\max\{p-n,0\}}$ characteristic functions on level p, which has to be multiplied with the number of "hyperbolic" tensor products with level p kept fixed.

In order to generalize our results to an isotropic 3d-wavelet basis, we have to introduce certain modifications. Instead of a single type of characteristic function, we have to deal with seven different types of wavelets $\gamma_{j\mathbf{a}}^{(p)}$ with $p=1,\ldots7$. As a consequence, the formulas (60), (62), (63), (64), and (65) have to be multiplied by weight factors 7^2, 7^2, 7^3, 7^3, and 7^4, respectively. On each level, the various types of wavelets are centered on regular grids, however, these grids are generically shifted to each other for

28

different types of wavelets. Furthermore, these shifts affect the overlaps between wavelets of the same type on different levels. This yields additional overlaps which are not taken into account by the model. The additional overlaps increase the constants in the formulas (60), (62), (63), (64), and (65) but otherwise do not affect the asymptotic behaviour. We have further assumed that there is no overlap between characteristic functions on the same level. For wavelets with compact support, this is obviously not satisfied in general. Depending on its regularity, a wavelet has nonvanishing overlap with the supports of a certain number of neighboring wavelets on the same level. Since the number of overlaps does not depend on the specific level, this enters in leading order as a multiplicative constant into our formulas.

D   Supplement to the recurrence scheme

In order to complete our presentation of the recurrence scheme, we provide the remaining steps in Figs. 15, 16, 17, 18, 19, and 20.
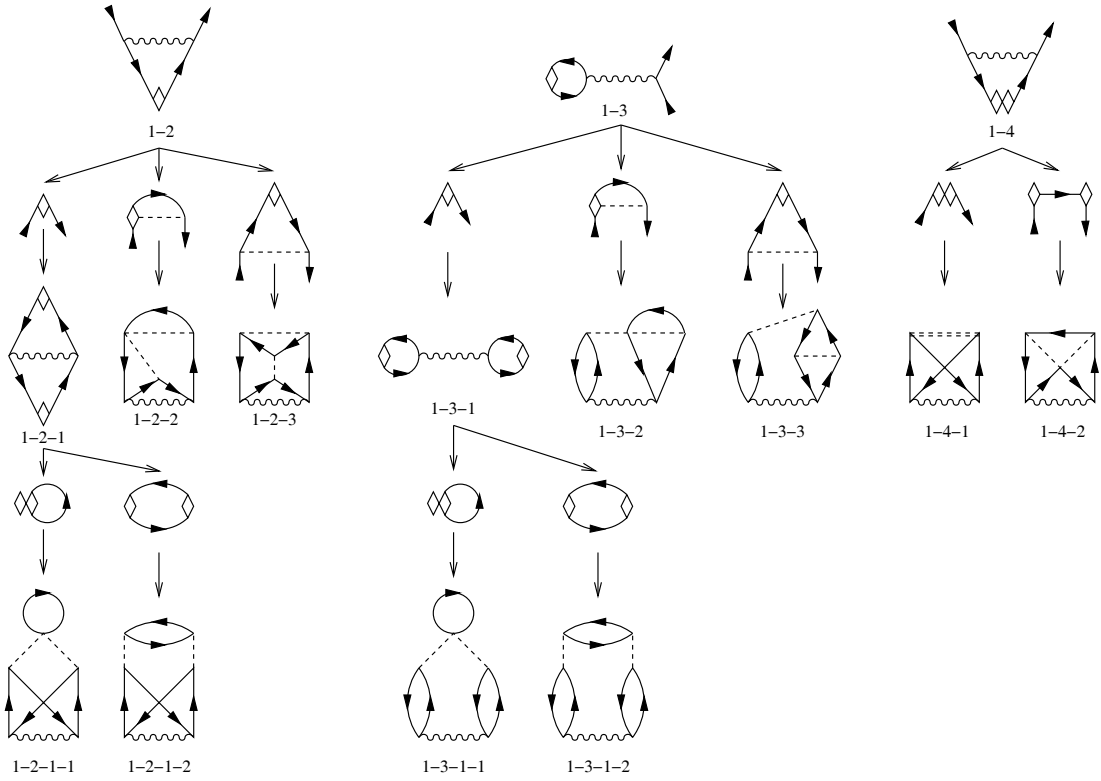

Figure 15: Recurrence scheme for diagrams emerging from sets of type 1-2 to 1-4 diagrams.
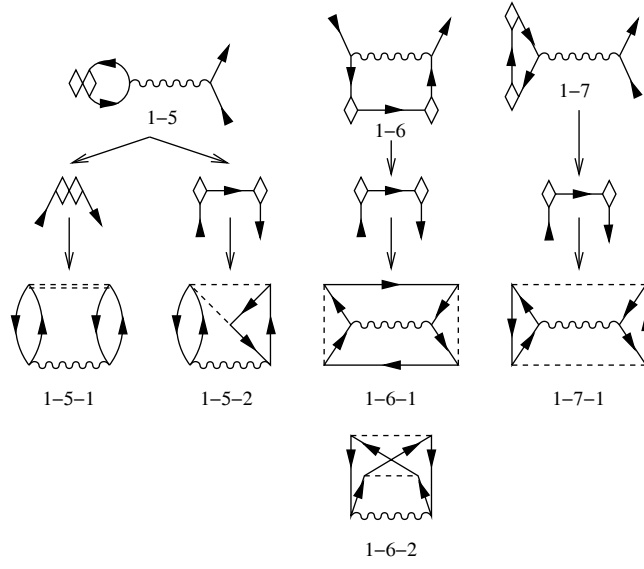
Figure 16: Recurrence scheme for diagrams emerging from sets of type 1-5 to 1-7 diagrams.
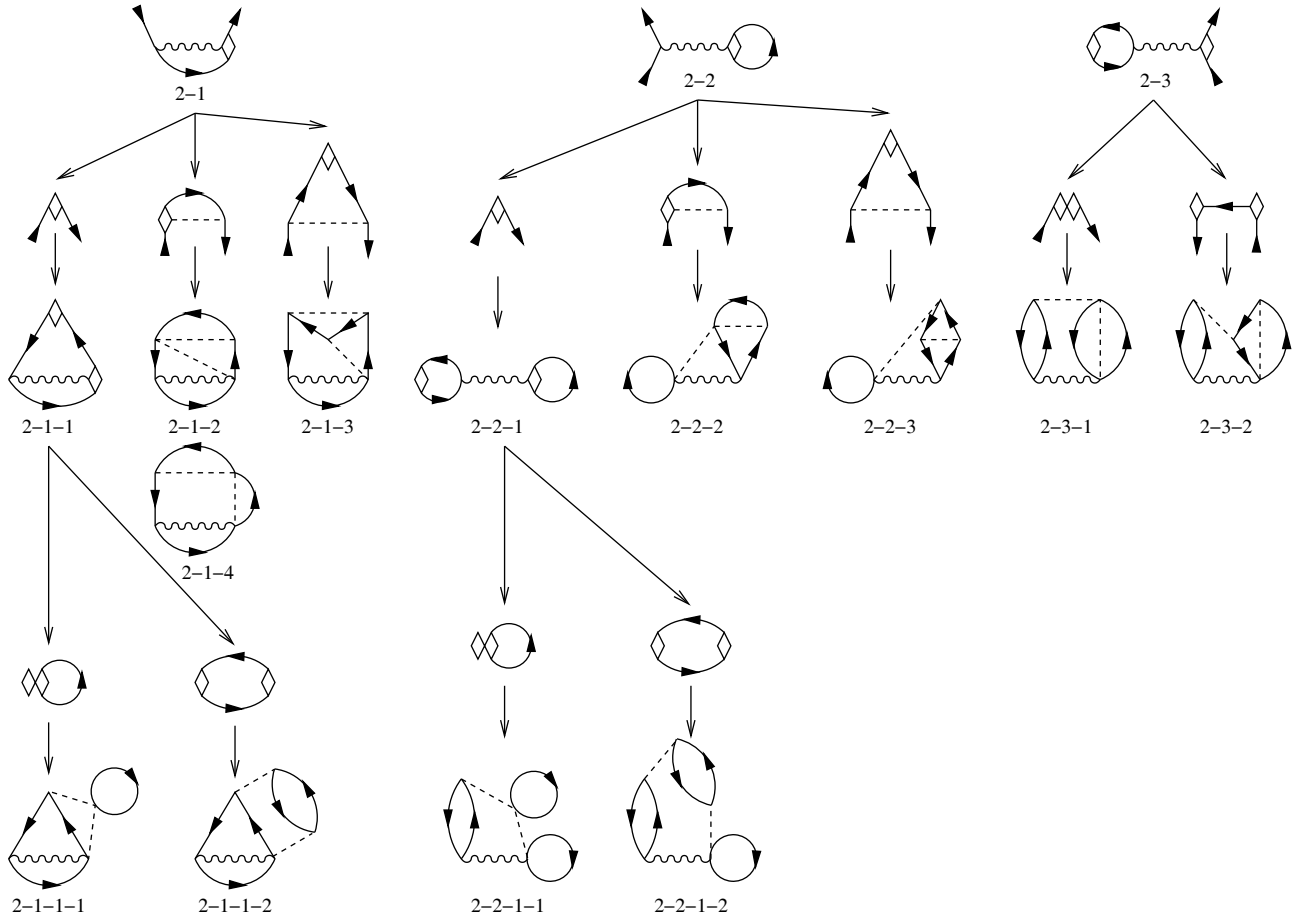

Figure 17: Recurrence scheme for diagrams emerging from sets of type 2-1 to 2-3 diagrams.
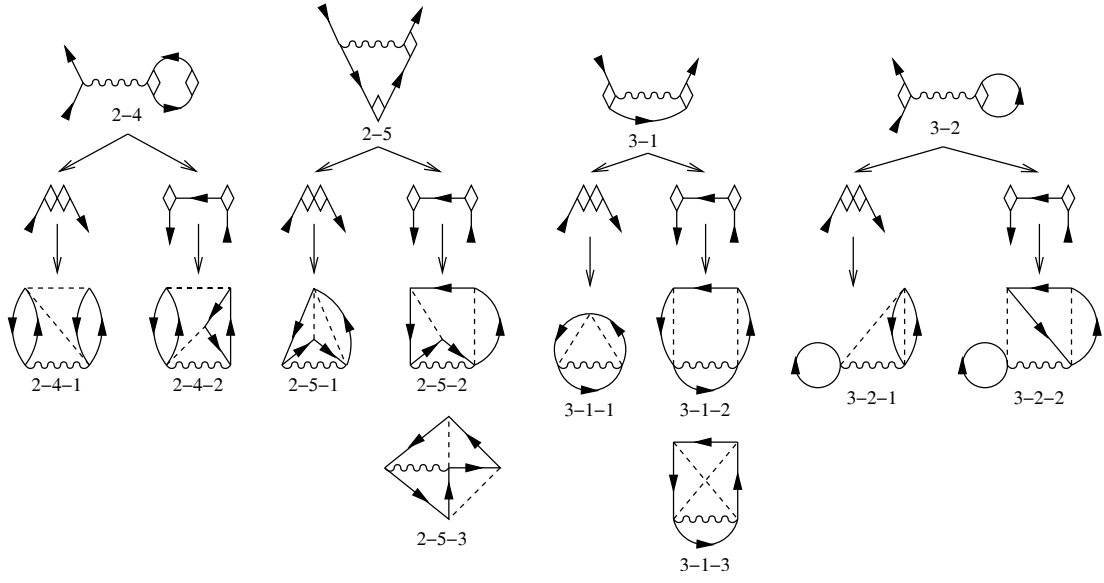
Figure 18: Recurrence scheme for diagrams emerging from sets of type 2-4, 2-5, 3-1, and 3-2 diagrams.
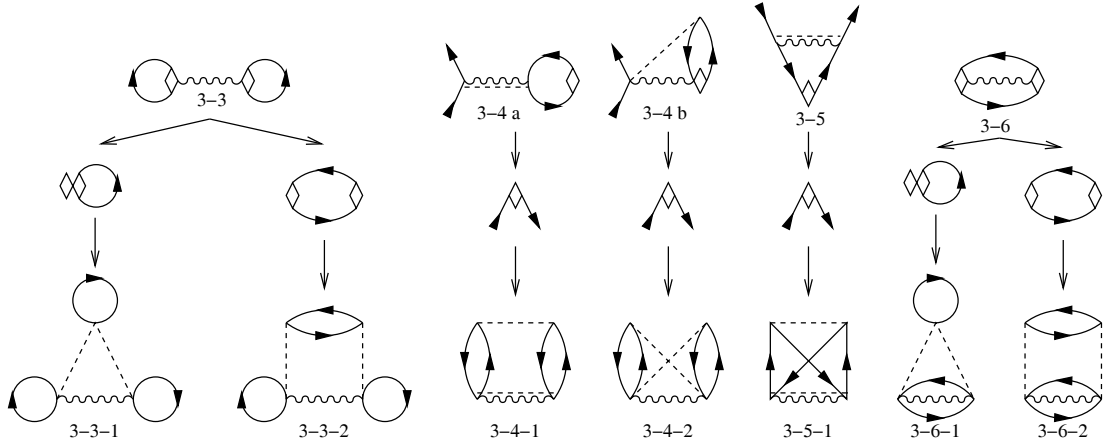

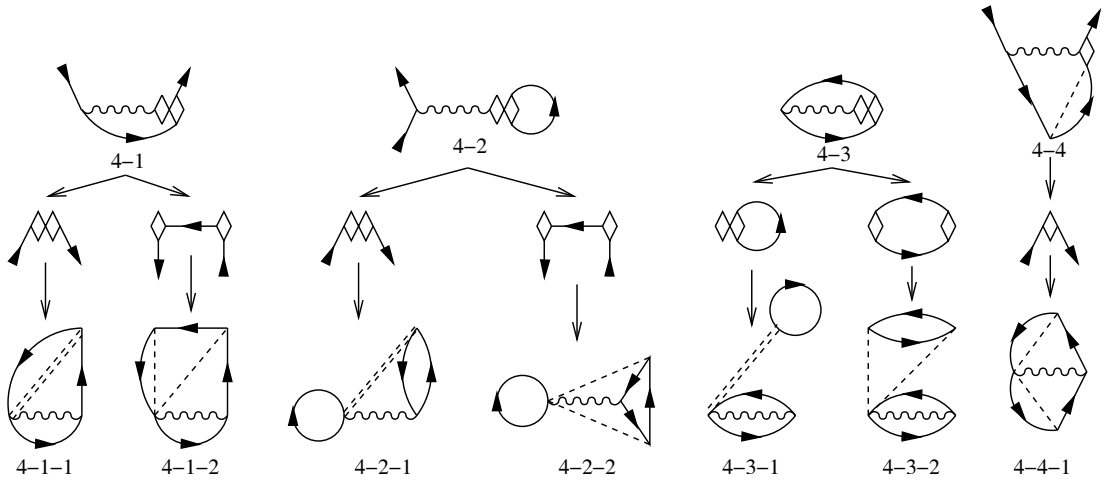Figure 19: Recurrence scheme for diagrams emerging from sets of type 3-3 to 3-6 diagrams.

Figure 20: Recurrence scheme for diagrams emerging from sets of type 4-1 to 4-4 diagrams.

31

References

[1] W. E and B. Engquist, Notices Amer. Math. Soc., **50**, 1062 (2003).

[2] I. Daubechies, *Ten Lectures on Wavelets*, CBMS-NSF Regional Conference Series in Applied Mathematics **61** (1992)

[3] Y. Meyer *Wavelets and Operators* (Cambridge University Press, 1992).

[4] Y. Meyer and R. Coifman, *Wavelets, Calderón-Zygmund and Multilinear Operators* (Cambridge University Press, 1997).

[5] S. Mallat, *A Wavelet Tour of Signal Processing* (Academic Press, San Diego, 1998).

[6] W. Dahmen, Acta Numerica **6**, 55 (1997).

[7] R.A. DeVore, Acta Numerica **7**, 51 (1998).

[8] S. Goedecker, *Wavelets and their Application for the Solution of Differential Equations*, (Presses Polytechniques Universitaires et Romandes, Lausanne, 1998).

[9] G. Beylkin, R.R. Coifman and V. Rokhlin, Commun. Pure Appl. Math. **44**, 141 (1991).

[10] G. Beylkin, SIAM J. Numer. Anal. **6**, 1716 (1992).

[11] W. Dahmen, S. Prößdorf, R. Schneider, Math. Z. **215**, 583 (1994).

[12] W. Dahmen, S. Prößdorf, R. Schneider, Adv. Comp. Maths. **1**, 259 (1993).

[13] A. Cohen, W. Dahmen and R.A. DeVore, Math. Comp. **70**, 27 (2001).

[14] K. Cho, T.A. Arias, J.D. Joannopoulos and P.K. Lam, Phys. Rev. Lett. **71**, 1808 (1993).

[15] S. Wei and M.Y. Chou, Phys. Rev. Lett. **76**, 2650 (1996).

[16] C.J. Tymczak and X.-Q. Wang, Phys. Rev. Lett. **78**, 3654 (1997).

[17] R.A. Lippert, T.A. Arias and A. Edelman, J. Comput. Phys. **140**, 278 (1998).

[18] S. Goedecker and O. Ivanov, Solid State Commun. **105**, 665 (1998).

[19] S. Goedecker and O. Ivanov, Comput. Phys. **12**, 548 (1998).

[20] S. Goedecker and O.V. Ivanov, Phys. Rev. B **59**, 7270 (1999).

[21] S. Han, K. Cho and J. Ihm, Phys. Rev. B, **60**, 1437 (1999).

[22] T.A. Arias, Rev. Mod. Phys. **71**, 267 (1999).

[23] J.-P. Antoine, Ph. Antoine and B. Piraux, in *Wavelets in Physics*, Ed. J.C. van den Berg (Cambridge University Press, Cambridge, 1999) p. 299.

[24] T.D. Engeness and T.A. Arias, Phys. Rev. B **65**, 165106 (2002).

[25] A.M.N. Niklasson, C.J. Tymczak and H. Röder, Phys. Rev. B **66**, 155120, (2002).

[26] K.S. Thygesen, M.V. Bollinger and K.W. Jacobsen, Phys. Rev. B **67** 115404 (2003).

[27] G. Frantziskonis and P. Deymier, Phys. Rev. B **68**, 024105, (2003).

[28] R.J. Harrison, G.I. Fann, T. Yanai and G. Beylkin, in *Computational Science - ICCS 2003*, LNCS **2660**, Eds. P.M.A. Sloot et al. (Springer, Berlin, 2003) p. 103.

[29] H.-J. Flad, W. Hackbusch, D. Kolb and R. Schneider, J. Chem. Phys. **116**, 9641 (2002).

[30] H. Luo, D. Kolb, H.-J. Flad, W. Hackbusch and T. Koprucki, J. Chem. Phys. **117**, 3625 (2002).

[31] J.W. Clark, in *Progress in Nuclear and Particle Physics Vol. 2*, Ed. D. H. Wilkinson (Pergamon, Oxford, 1979) p. 89.

[32] R.A. DeVore, S.V. Konyagin and V.N. Temlyakov, Constr. Approx. **14**, 1 (1998).

[33] W. Duch and G.H.F. Diercksen, J. Chem. Phys. **101**, 3018 (1994).

[34] W. Hackbusch, Computing **67**, 35 (2001).

[35] T. Helgaker, P. Jørgensen and J. Olsen, *Molecular Electronic-Structure Theory* (Wiley, New York, 1999).

[36] D.E. Woon and T.H. Dunning, Jr., J. Chem. Phys. **100**, 2975 (1994).

[37] W. Kutzelnigg, in *Methods of Electronic Structure Theory*, Vol. 3 of *Modern Theoretical Chemistry*, Ed. H.F. Schaefer III (Plenum, New York, 1977), p. 129.

[38] S. Saebø and P. Pulay, Annu. Rev. Phys. Chem. **44**, 213 (1993).

[39] M. Schütz, G. Hetzer and H.-J. Werner, J. Chem. Phys. **111**, 5691 (1999).

[40] M. Schütz and H.-J. Werner, J. Chem. Phys. **114**, 661 (2001).

[41] E. Krotscheck, Ann. Phys. **155**, 1 (1984).

[42] E. Krotscheck, Phys. Rev. B **31**, 4267 (1985).

[43] G. Stollhoff and P. Fulde, J. Chem. Phys. **73**, 4548 (1980).

[44] G. Stollhoff, J. Chem. Phys. **105**, 227 (1996).

[45] R.F. Bishop, Theoret. Chim. Acta **80**, 95 (1991).

[46] E. Krotscheck, W. Kohn and G.-X. Qian Phys. Rev. B **32**, 5693 (1985).

[47] T. Pang, C.E. Campbell and E. Krotscheck, Chem. Phys. Lett. **163**, 537 (1989).

[48] C.E. Campbell, E. Krotscheck and T. Pang, Physics Reports **223**, 1 (1992).

[49] P. Fulde, *Electron Correlations in Molecules and Solids* (Springer, Berlin, 1993).

[50] K.W. Becker and P. Fulde, J. Chem. Phys. **91**, 4223 (1989).

[51] J.D. Talman, Phys. Rev. A, **10**, 1333 (1974).

[52] I. Lindgren and J. Morrison, *Atomic Many-Body Theory* (Springer, Berlin, 1986).

[53] S. Goedecker, Rev. Mod. Phys. **71**, 1085 (1999).

[54] A.J. Stone, *The Theory of Intermolecular Forces* (Clarendon, Oxford, 1996).

[55] J.D. Talman, Phys. Rev. A, **13**, 1200 (1976).

[56] D. Ceperley, Phys. Rev. B **18**, 3126 (1978).

[57] D. Braess, J. Approx. Theory **83**, 93 (1995).

[58] W. Sweldens, Appl. Comp. Harm. Anal. **3**, 186 (1996).

[59] G. Deslauriers and S. Dubuc, Constr. Approx. **5**, 49 (1989).

[60] C. Zenger, in Parallel Algorithms for Partial Differential Equations: Proceedings of the Sixth GAMM-Seminar, Kiel, January 1990, Notes on Numerical Fluid Mechanics (Vol. 31), edited by W. Hackbusch (Vieweg, Braunschweig, 1991).

[61] H.-J. Bungartz, in Iterative Methods in Linear Algebra, edited by P. de Groen and R. Beauwens (Elsevier, Amsterdam, 1992) pp. 293-310.

[62] R. Balder and C. Zenger, SIAM J. Sci. Comput. **17**, 631 (1996).

[63] J. Garcke and M. Griebel, J. Comp. Phys. **165**, 694 (2000).

[64] M. Griebel and S. Knapek, Constr. Approx. **16**, 525 (2000).

[65] T. Gerstner and M. Griebel, Computing **71**, 65 (2003).